JQS Journal of Quaternary Science QRA Quaternary Research Association

Ground truth validated 3D electrical resistivity imaging of the archaeological deposits at Arma Veirana cave (northern Italy)

P. TORRESE,[1]* F. ZUCCA,[1] S. MARTINI,[2] S. BENAZZI,[3,4] D. DROHOBYTSKY,[5] C. GRAVEL-MIGUEL,[6,7] J. HODGKINS,[8] D. MEYER,[5] C. MILLER,[9,10] M. PERESANI,[11,12] C. ORR,[8] J. RIEL-SALVATORE,[7] D. S. STRAIT[13,14] and F. NEGRINO[15]

[1]Dipartimento di Scienze della Terra e dell'Ambiente, Università di Pavia, Pavia, Italy
[2]GEA Servizi di Geoarcheologia Srls, Mornico Losana, Pavia, Italy
[3]Dipartimento di Beni Culturali, Università di Bologna, Ravenna, Italy
[4]Department of Human Evolution, Max Planck Institute for Evolutionary Anthropology, Leipzig, Germany
[5]Cultural Heritage Engineering Initiative (CHEI), University of California San Diego, La Jolla, CA, USA
[6]School of Human Evolution and Social Change, Institute of Human Origins, Arizona State University, Tempe, AZ, USA
[7]Département d'Anthropologie, Université de Montréal, Montréal, QC, Canada
[8]Department of Anthropology, University of Colorado, Denver, CO, USA
[9]Institute for Archaeological Sciences and Senckenberg Centre for Human Evolution and Paleoenvironment, University of Tübingen, Tübingen, Germany
[10]SFF Centre for Early Sapiens Behaviour (SapienCE), University of Bergen, Bergen, Norway
[11]Dipartimento di Studi Umanistici, Sezione di Scienze Preistoriche e Antropologiche, Università di Ferrara, Ferrara, Italy
[12]Istituto di Geologia Ambientale e Geoingegneria, Consiglio Nazionale delle Ricerche, Milano, Italy
[13]Department of Anthropology, Washington University in St. Louis, St. Louis, MO, USA
[14]Palaeo-Research Institute, University of Johannesburg, Auckland Park, Gauteng, South Africa
[15]Dipartimento di Antichità, Filosofia, Storia (DAFIST), Università di Genova, Genova, Italy

ABSTRACT: We present 3D electrical resistivity tomography (ERT) imaging of the archaeological deposits at Arma Veirana cave (northern Italy), to date only partially explored. The archaeological importance of the cave is due to the presence of a rich Mousterian layer, traces of Late Upper Palaeolithic (Epigravettian) temporary occupations and an Early Mesolithic burial of a female newborn. ERT is rarely employed in Palaeolithic cave contexts because Palaeolithic remains are typically disseminated in loose deposits and either do not possess high electrical resistivity contrasts or are too small to be detected. Furthermore, some issues can derive from the confined environment in caves. In this view, our study represents an opportunity to assess the capability of this geophysical method to retrieve subsurface information of Palaeolithic cave deposits and create a framework for the improvement of ERT applications in such a peculiar cave context. The aim of this study was to define the features of the deposits (i.e. geometry, thickness and sediment distribution) and to map the morphology of the underlying bedrock. Results reveal that the thickness of the deposits varies both along the primary axis of the cave and transverse to it. This study allowed the recognition of shallow, meter-sized, fine-grained sediment-filled structures with a longitudinal orientation with respect to the primary axis of the cave, as well as a possible erosional-like structure. The cross-validation of geophysical results with the archaeological evidence (the Early Mesolithic newborn burial and Epigravettian artefacts) confirms that the low-resistivity unit could be the most promising from an archaeological point of view.
© 2022 John Wiley & Sons, Ltd.

KEYWORDS: 3D resistivity imaging; cave deposit; Early Holocene; ERT; geophysical investigations; Pleistocene

Introduction

In general, one of the primary goals of a new archaeological excavation project is to document the formation of the site, as well as the extent of its deposit. At the Arma Veirana cave, which is the topic of the present study, only a small portion of the deposit has been explored during the four recent archaeological field seasons (Negrino *et al.*, 2018; Hodgkins *et al.*, 2021). While recent documentations of exposed sections have provided a fair amount of data on some of the depositional history at the front of the cave, the depth and richness of the sediment remained unknown for all portions of the cave. Given the destructive nature of archaeological excavations, non-destructive in-depth investigation of the deposits is a valuable approach to help design

future excavations. Specifically, at this point in the project, it became important to assess the extent and define the properties and volumes of potential artefact-bearing deposits before proceeding with further excavation.

In this context, the team turned to near-surface geophysical methods as an important tool to derive key information about underground properties and structures. Geophysical methods are an important component of geoarchaeological investigations. They allow non-invasive and rapid imaging of archaeological settings and help answer scientific questions by considering a site integrally within its geological surroundings. They are particularly useful in geoarchaeological investigations to define site stratigraphy, map site disturbance and reconstruct palaeolandscapes (Sarris *et al.*, 2018). However, geophysical techniques are seldom used to investigate Palaeolithic archaeological sites (Obradovic *et al.*, 2015;

*Correspondence: P. Torrese, as above.
E-mail: patrizio.torrese@unipv.it

Abu Zeid et al., 2019), mostly due to those sites' sedimentary nature and the almost complete absence of architectural remains that can result in clear geophysical anomalies. The presence of numerous, thin and closely packed occupation layers containing archaeological remains that are generally very small and would be destroyed by invasive investigations makes the contribution of geophysical methods significant (cf. Abu Zeid et al., 2019). Schmidt et al. (2015) provide an overview of the issues to be considered when undertaking or commissioning geophysical surveys in archaeology.

One of the most frequently used geophysical techniques is electrical resistivity tomography (ERT). It is a quick and cost-effective method that provides reliable imaging of the subsurface electrical resistivity pattern and allows identification of underground structures. ERT theory (cf. Dahlin and Loke, 1998; Loke et al., 2003) and application (cf. Griffiths and Barker, 1993; Guerin and Benderitter, 1995; Torrese, 2020; Torrese et al., 2021a) are well documented in geophysical research literature.

ERT is widely used in archaeological studies (Campana and Piro, 2008; Witten, 2017; El-Qady et al., 2019). It has been used to investigate site stratigraphy (Papadopoulos et al., 2006) and the sedimentological architecture (Yogeshwar et al., 2019), to detect changes in lithology and geology (Laigre et al., 2012; Scapozza and Laigre, 2014), depositional targets and buried structures (Papadopoulos et al., 2007; Tsokas et al., 2009; Supriyadi et al., 2019; Cozzolino et al., 2020), to map remnants of past human occupation (Thacker et al., 2002; Matias et al., 2006; Papadopoulos et al., 2010; Berge and Drahor, 2011a,b; Tsokas et al., 2018), to reconstruct palaeolandscapes (Papadopoulos et al., 2014) as well as to detect offshore archaeological features (Sarris et al., 2014; Tonkov, 2014; Simyrdanis et al., 2015). ERT is also widely used to choose the most promising areas to excavate (Piroddi et al., 2020).

Palaeolithic caves in temperate regions of Europe are often filled with deposits that are poorly sorted and display a wide range of grain sizes, from large blocks of roof fall (éboulis) to silt and clays (Goldberg and Sherwood, 2006; Mallol and Goldberg, 2017). Differently from other archaeological settings with localized and large anomalies easily detectable by ERT, the Palaeolithic remains contained in such loose deposits are disseminated and either do not possess high electrical resistivity contrasts or are too small to be detected. This explains why ERT is rarely employed in Palaeolithic cave contexts. Furthermore, given that the depth of investigation provided by ERT is tied to the length of the electrode array deployed, some issues can derive from the confined environment in caves (cf. Abu Zeid et al., 2019).

Previous geophysical studies performed in Palaeolithic caves focused mainly on retrieving the cave geometry and investigating the presence of voids (Beck and Weinstein-Evron, 1997; Jol et al., 2002; Quarto et al., 2007; Shopov et al., 2008). To our knowledge, ERT-based studies meant to document the features of the deposits and map the morphology of the underlying bedrock of Palaeolithic caves are so far limited (Abu Zeid et al., 2019).

In this view, our ERT-based study of the archaeological deposits at Arma Veirana cave represents an opportunity to assess the capability of this geophysical method to retrieve subsurface information of Palaeolithic cave deposits and create a framework to improve ERT applications in such a peculiar context. As primary goals, the study aimed to create a three-dimensional (3D) resistivity model of the archaeological deposits at Arma Veirana cave, to identify the volume of the deposits (or sediments, defined as detrital, loose, explorable materials, i.e. grains of clay, silt, sand and gravel) with the highest archaeological potential in terms of geometry, thickness and sediment distribution, and to map the morphology of the bedrock. This work leads to methodological insights about how to improve both the efficiency and effectiveness of future archaeological campaigns inside caves, especially suitable for the Palaeolithic age. New insights on the development of Arma Veirana cave and on the nature of its sedimentary infill are also provided, thereby enabling a better understanding of the depositional processes involved in the formation of this important archaeological site. This information will be useful in the planning of long-term field-investigations and to locate areas that should be the focus of future excavations.

The ERT technique and the resistivity signature of the target

ERT is based on a multi-electrode system applying direct current into the ground by means of two current electrodes and measures the resulting voltage via two potential electrodes; each of the electrodes alternatively acts as a current and potential electrode. To obtain a true resistivity model of the subsurface, an inversion procedure is needed (Loke and Barker, 1996). The arrangement of current and potential electrodes during the measurement is dependent on the chosen electrode array. The most frequently used arrays are the dipole–dipole, Wenner and Wenner–Schlumberger arrays (e.g. Kneisel, 2006; Schrott and Sass, 2008). The dipole–dipole array uses two current electrodes on one side and two potential electrodes on the other side. This method is especially suitable for the detection of vertical structures, as it shows high lateral resolution, but it is too sensitive to near-surface anomalies (Szalai and Szarka, 2008). The Wenner array comprises four equally spaced electrodes deployed in a line in which potential electrodes are located between current electrodes. The method is especially suitable for the detection of horizontal structures as it shows high vertical resolution, but it has shallower penetration and less subsurface information than the dipole–dipole array (Szalai et al., 2009). The Wenner–Schlumberger array is similar to the Wenner array; potential electrode spacing is constant but current electrode spacing is logarithmically increased. This array is especially appropriate for the detection of horizontal structures since it shows high vertical resolution like the Wenner array, but it has shallower penetration and less subsurface information than the dipole–dipole array. As each array has different disadvantages, we combined all of them here to go beyond their individual limits and obtain more accurate models.

ERT allows the characterization of subsurface materials based on their electrical properties. Changes in electrical resistivity correlate with variation in solid material (minerals and rocks), water saturation, fluid conductivity and porosity, which may be used to map stratigraphic units, geological structure, fractures, groundwater and anthropogenic structures. ERT has been successfully used to identify and map low-resistivity volumes such as fine-grained archaeological deposits (Abu Zeid et al., 2019; Becker et al., 2019), as well as typically high-resistivity structures, including bedrock, wall pipes, roads (Tsokas et al., 2009), foundations (Drahor et al., 2008), ditches, palaeochannels, internal structures in mounds and barrows (Astin et al., 2007; Papadopoulos et al., 2010), buried chambers and cavities (Cardarelli et al., 2006; Deiana et al., 2018), caves, karst features, sinkholes and cavities (e.g. Smith, 1986; Maillol et al., 1999; Van Schoor, 2002; Al-Zoubi et al., 2007; Ortega et al., 2010; Zhu et al., 2011; Carrière et al., 2013; Satitpittakul et al., 2013; Rainone et al., 2015; Torrese, 2020; Torrese et al., 2021a), and offshore archaeological features (Sarris et al., 2014; Tonkov, 2014; Simyrdanis et al., 2015).

One of the most important targets of ERT application in archaeological studies is the depth to the bedrock. Accurate information about bedrock morphology and depth can vastly improve excavation planning. Bedrock and sediments have typically different electrical resistivity; therefore, the bedrock's buried surface can be measured as a high-contrast boundary in an electrical resistivity model. In the case of irregular morphology of bedrock, 3D ERT is required to build a more complete and accurate model.

The resistivity signature of the target depends on its size in relation to its depth and on the contrast between its resistivity and that of the surrounding (host) rock. The amplitude of resistivity anomalies is an inverse function of the distance between the measurement points and the cavity. The depth of investigation and the vertical and horizontal resolutions of ERT surveys are linked to: (i) the electrode spacing, (ii) the configuration array, (iii) the quadrupole sequence, (iv) the signal-to-noise ratio (SNR), (v) the contrast between the resistivity of the target and (vi) the surrounding rock and/or background resistivity.

The ERT method has been applied at Arma Veirana cave because it is particularly effective in such a geological setting (i.e. where the target deposits consist mainly of fine deposits bounded below and laterally by limestone rocks). In this context, we expected ERT to provide an accurate model of the depth and position of the archaeological deposits thanks to their low resistivity while the host rocks are of high resistivity.

ERT application inside caves

Applying ERT inside caves (Hancock, 1999; Pringle et al., 2002; Abu Zeid et al., 2019; Olenchenko et al., 2019; Osipova et al., 2020) entails several issues caused by limited space for measurements and the complexity of the surrounding medium's structure as compared to above-ground measurements. Olenchenko et al. (2020) performed numerical experiments to assess the effect of the 3D cave geometry on the results of an ERT inversion. They found that variations of cave geometry parameters result in unexpected false anomalies, and that considerable errors in bedrock location and resistivity can occur. The authors suggested that two-dimensional (2D) ERT generally cannot be applied inside a cave whose half-width is smaller than the thickness of sediments; 3D surveys do not essentially improve the quality of results.

Findings from Olenchenko et al. (2020) on the use of ERT inside caves are consistent with results obtained by Fikos et al. (2019) who evaluated the ability of 2D ERT to provide effective results along profiles undertaken close and parallel to the vertical cave walls. By combining numerical modelling with field data, the authors found that if the distance between ERT profiles and the cave walls becomes too small, the high resistivity of the cave walls masks the conductive sediment layer. Furthermore, the resistivity of the sediments is significantly overestimated, thus posing possible problems in the interpretation process.

However, as suggested by Olenchenko et al. (2020), in the case of downward diverging cave walls, as occurs at Arma Veirana cave (Fig. 1), an accurate resistivity model can be obtained. In such a case, despite being within a 3D cave geometry, the electric current is distributed approximately as in a 2D medium. Therefore, ERT in caves with similar geometry can yield reliable results on the morphology of the bedrock surface, the thickness of sedimentary layers, and the size and position of inclusions such as fallen fragments of roof therein. Under these conditions, 3D surveys improve the quality of results, thus providing more complete and accurate models than 2D surveys.

ARMA VEIRANA

Arma Veirana, also known as Arma della Costa di Cerisola (Dal Bo et al., 1978), is located in the municipality of Erli, in the Savona province (Liguria, northern Italy). It is situated in calcareous rocks of the Castelvecchio–Cerisola Unit of the Ligurian Briançonnais domain (Decarlis and Lualdi, 2009) and consists of a SE/NW-orientated chamber 44 m long with an upslope of 4 m between the cave entrance and its termination (Fig. 1).

The archaeological importance of the cave was first recognized in 2006 by Giuseppe Vicino, curator of the Museo Archeologico del Finale (Savona), who collected Middle and Upper Palaeolithic artefacts from the removed deposit. Formal excavations began in 2015 and lasted until 2018.

To date, the main objective of the archaeological fieldwork has been to document the cave's stratigraphy, which was initially visible in pits exposed by looters. Excavations at Arma Veirana have focused on several locations within the cave, exposing stratigraphic sections that span several lithological units referred to as stratigraphic aggregates (StratAggs) in our excavation system (equivalent to what are often called 'layers'). The excavations exposed a rich Mousterian layer at the bottom of the main trench (stratigraphic section a–b, Fig. 2), which is located near the entrance of the cave, and traces of Late Upper Palaeolithic (Epigravettian) occupations in the upper aggregates. As reported in Hodgkins et al. (2021), an Early Mesolithic burial (10.280–9.924 cal BP) of a 40–50-day-old female newborn (AVH-1, nicknamed 'Neve') was recovered in 2017 within an approximately 15-cm-deep oval pit (<600 cm^2 in area) cut into underlying late Epigravettian deposits. The burial feature containing the newborn remains was exposed after removing a thin layer of surficial deposits and appears to be intrusive into the underlying stratigraphic aggregate 'Yellow Silt' (YS).

Numerous radiocarbon dates have been obtained, DNA samples collected and traces of cryptotephra identified in correspondence of the Middle Palaeolithic layers (Hirniak et al., 2020). Analysis of the archaeological finds and other geoarchaeological evidence is underway.

Geological and archaeological setting of the cave

Geologic setting

The entrance of the Arma Veirana cave is located in a tight antiform syncline (Goudie, 2013) (interlimb angle > 30°) at the stratigraphic contact (Dallagiovanna et al., 2011) between the Val Tanarello limestone of the Kimmeridgian–Berriasian age (Bertok et al., 2011) at the top and the calcareous schists and shales of the Caprauna Formation of late Cretaceous–middle Palaeogene period (Dallagiovanna et al., 2011) at the bottom; it is an uncommon case of an inner-fold cave, where the access opening corresponds to a rock fall related to the Rio Neva valley evolution (Fig. 1d).

With regard to the cave genesis and evolution, we identify here the model that best fits with field observations and the results of the geophysical investigation. In brief, even if carbonate dissolution may have had some role in the first stage of its development (Dubois et al., 2011; Quinif, 2014, 2018), Arma Veirana is not an epigenetic solution cave. According to the most recent classification (Oberender and Plan, 2018) it is a 'pseudo-endokarst' produced first by 'mechanical weathering' (first-order type cave genesis according to Quinif and Bruxelles, 2011) followed by alterite removed through 'piping' (second-order cave genesis) with
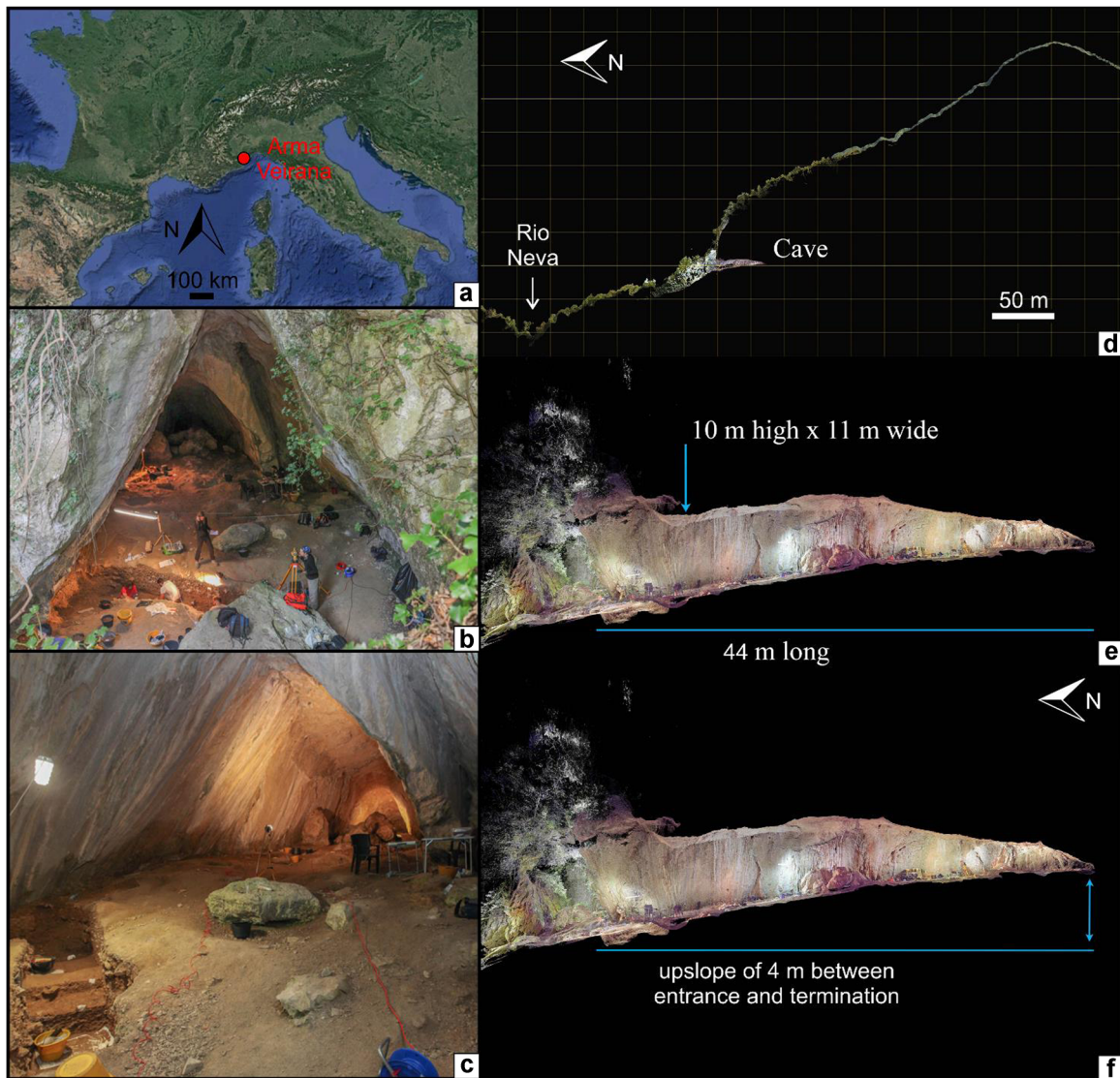
Figure 1. Arma Veirana: (a) geographical setting, (b) picture from outside the cave, (c) picture from inside the cave, (d) location of the cave in cross-section with respect to the slope and Rio Neva, (e,f) cross-section and geometric features of the cave; the cross-sections (d–f) were derived from a LiDAR reconstruction of the cave. [Color figure can be viewed at wileyonlinelibrary.com]

the final development of a 'suffusion cave' (Sauro, 2005; Sola, 2007).

Speleogenesis models of Veirana cave, its relationships with the palaeo-evolution of the Rio Neva palaeovalley, the development of the other caves and canyons of the area and their relations with prehistoric anthropic settlement are active areas of research.

Archaeological evidence

To document the history of the cave, several archaeological pits have been excavated in different parts of the cave, with the deepest trench dug near the entrance of the cave. This main trench is about 1.2 m deep but has not yet reached the bedrock. Yet, the sediments exposed by this trench have revealed interesting anthropic evidence pertaining to the Middle Palaeolithic. The stratigraphy of this trench consists of five distinct stratigraphic aggregates (or layers) named, from top to bottom: 'Disturbed' (D), 'Rocky Brown' (RB), 'Consolidated Strong Brown' (CSB), 'Granular' (Gr) and 'Black Mousterian' (BM) (Fig. 3 and Supporting Information, Fig. S1) that are differentiated from each other through variation in grain size, colour, fabric and structures. Radiocarbon dates

obtained on material from those aggregates show that they are older than 50 ky BP.

Anthropic evidence is mainly concentrated in the layer at the base of the currently exposed stratigraphy, the BM aggregate, a 20–30-cm-thick silty-sand layer with medium to small gravel with a dark greyish brown colour, due to the presence of manganese oxide staining but also numerous silt- and sand-sized fragments of combustion residues (e.g. charcoal). This aggregate has provided abundant fauna, which is often fragmented and bears anthropogenic cut marks, along with numerous Mousterian lithic artefacts (Middle Palaeolithic).

The aggregates above BM have lower artefact density, suggesting that the cave was not occupied as intensely during the accumulation of the deposit. The Gr is a narrow aggregate characterized by medium sandy silt with granules and gravel, with colour varying around 10YR 4/4 to 10YR 4/3 (brown to dark yellowish brown). It exhibits a coarse crumb structure. It has a relatively high proportion of éboulis, which is mostly dominated by subangular to subrounded clasts that appear weathered and are on average 5–10 cm in size. The proportion of éboulis decreases to the east, however, where éboulis is rarer. Portions of Gr appear cemented by secondary carbonate, forming a weak breccia.

Above Gr, the CSB is a clayey silt with fine sand and gravel. It appears more compact than Gr and displays a massive
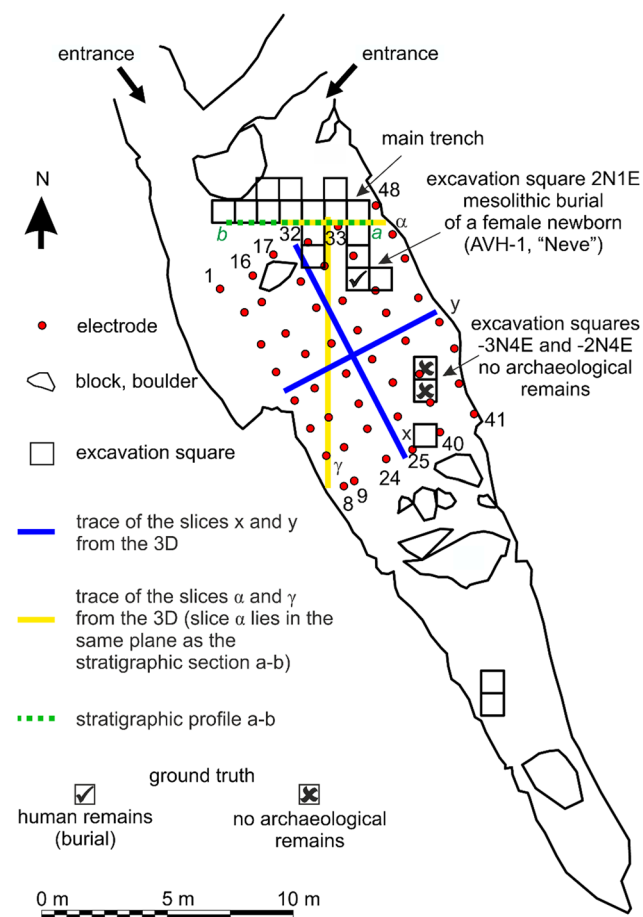
Figure 2. Experimental layout of the 3D ERT survey along with the traces of the slices and of the stratigraphic profiles, location of excavation pits and main archaeological material. [Color figure can be viewed at wileyonlinelibrary.com]
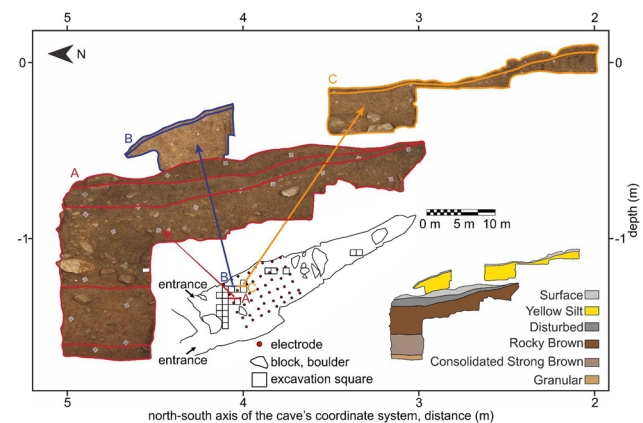

Figure 3. Photograph and stratigraphic drawing of N–S profile. The composite image is a projection of two profiles. The more western profile is located closer to an erosional rill, and therefore does not contain Yellow Silt (YS) aggregate, which is only exposed in excavations along the flank of the cave as represented in the more eastern profile. Excavations have exposed deposits (Black Mousterian, BM) below Granular (GR), but they have not yet been reached in the excavation units. [Color figure can be viewed at wileyonlinelibrary.com]

structure. The colour is dark yellowish brown (10YR 4/4). Larger blocks of éboulis are relatively rare and consist mostly of 5-cm-sized subangular to angular clasts which are locally organized into horizontally orientated lenses.

RB sits on top of CSB. RB is a clayey silt with fine sand and gravel and displays a weakly developed subangular blocks

structure; the color is dark yellowish brown (10YR 4/4). RB contains a relatively high proportion of subangular to angular blocks of éboulis which are generally 10–15 cm in size. These occur in higher proportion than in CSB.

An erosional unconformity distinguishes RB from the overlying D aggregate. D is a clayey silt with minor sand and gravel components with a dark greyish brown colour. It appears to be modern surficial deposits, which are expressed either as sedimentary infillings within the rill system or as alteration surfaces formed directly on RB.

Higher in the cave deposits, (south of the main excavation trench), the YS aggregate is a 20-cm-thick layer containing Late Upper Palaeolithic artefacts (Epigravettian). YS appears to be a clayey silt with minor sand and gravel components. Larger blocks of éboulis are rare, and most are between 5 and 7 cm in size. They appear subrounded and display no preferred orientation. The colour of YS is similar to RB (10YR 4/4) although it locally appears more yellowish. The Early Mesolithic burial was found inside a pit dug into the YS, ~2 m from the east wall of the cave (excavation square 2N1E in Fig. 2) (Hodgkins et al., 2021). YS was readily distinguishable from the burial pit which was darker in colour and had a high proportion of coarse material, including charcoal and bone.

The aforementioned erosional unconformity crosscuts several of the aggregates, so that towards the entrance of the cave D unconformably covers RB, whereas it covers YS towards the back and near the burial (Fig. 3). It is currently unknown whether the unconformity is local or cave-wide. Supporting Information Figure S1 provides detailed images of the aggregates.

Dates of stratigraphic aggregates reported in this paper derive from ^{14}C accelerator mass spectrometry (AMS) dating of faunal bone. Calibrations were done using IntCal20 (Reimer et al., 2020) in the OxCal 4.4 program (Bronk Ramsey, 2009).

Materials and methods

Data collection

3D ERT data were collected on 27 June 2018 with a fully automatic multi-electrode resistivity meter (SYSCAL Jr Switch-48, IRIS Instruments). A surface snake grid consisting of 8 × 6 electrodes spaced ~1.5 m apart both along the x- and y-axes was used (Fig. 2). The electrodes could not be placed in a perfectly regular grid due to the presence of blocks, boulders and calcite concretions on the ground (Fig. 4a–c). Despite this, the grid created allowed us to analyse an area of 10.5 × 7.5 m with a maximum depth of ~2 m.

Data were collected using different electrode arrays: 202 dipole–dipole (DD) measures, 96 Wenner (W) measures, 134 Wenner–Schlumberger (WS) measures and 328 Pseudo Pole-Dipole measures (PsPD), for a total of 760 quadrupole measures for the whole model. The PsPD array was comprised two remote electrodes (one for forward and the other for reverse measurements, aligned along the axis of the cave) placed 25 m away from the centre of the grid (Fig. 4d). Because it uses a remote electrode with a finite distance location instead of a remote electrode with an infinite distance location provided for by theoretical pole–dipole (Robain et al., 1999; Razafindratsima and Lataste, 2014), this array has been named pseudo pole–dipole rather than pole–dipole. Only forward measurements (no reverse measurements) were simulated with the PsPD array.

The data obtained with these arrays differed in resolution. Following Szalai et al. (2009), they were merged to deliver better detectability and imaging and, therefore, provide more accurate inverse models.
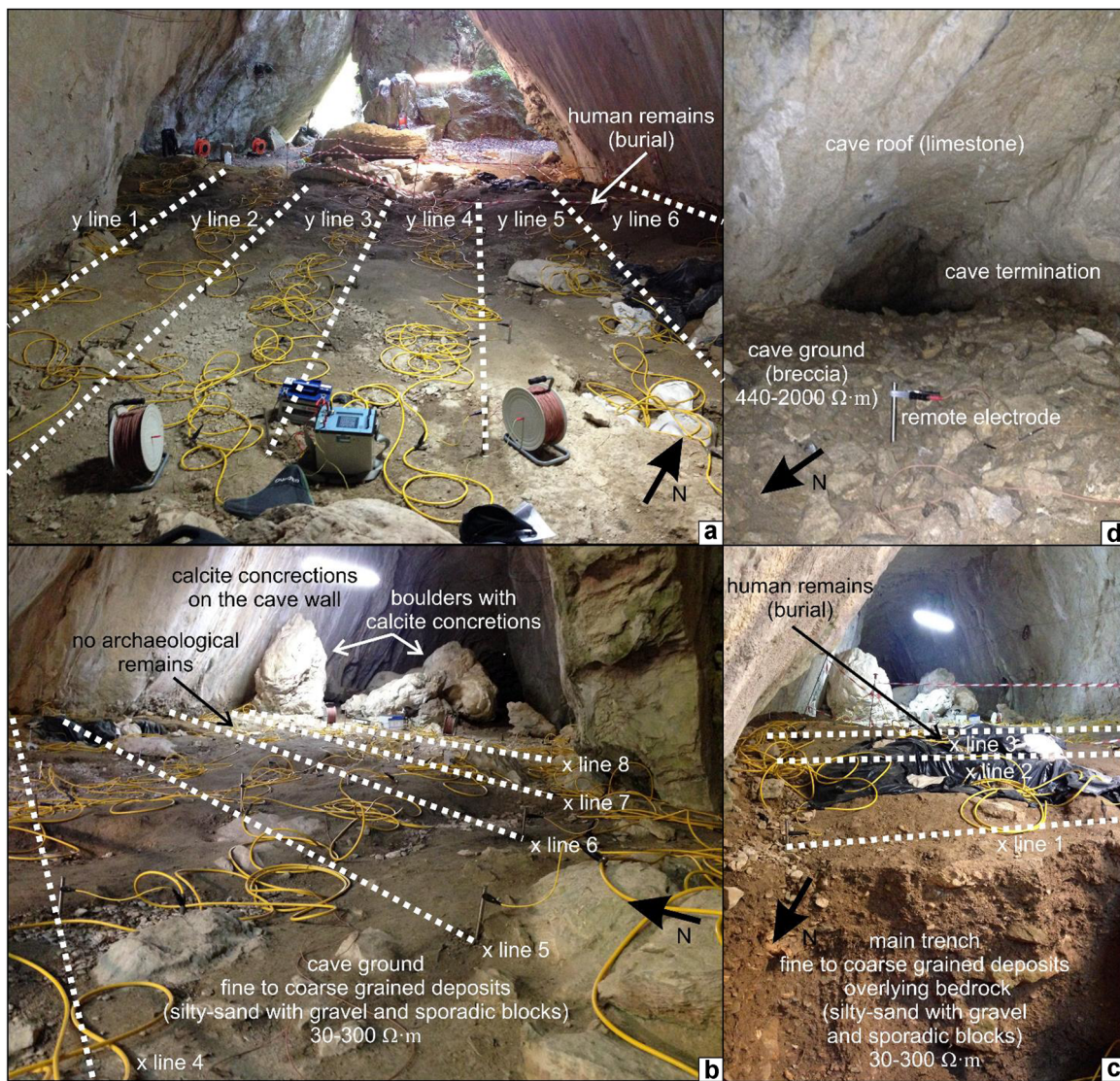
Figure 4. Pictures showing different views of the 3D ERT survey grid along with lithological descriptions. [Color figure can be viewed at wileyonlinelibrary.com]

Details on raw data quality are provided in Supporting Information Table S1.

Data inversion

No data processing (pre-inversion) was required to remove outliers from apparent (raw) resistivity data. The dataset, in fact, does not present any problematic data such as unrealistically high resistivity (>10 000 $\Omega \cdot m$) or too-high standard deviation (>10 $\Omega \cdot m$).

Then, ERTLab Solver (Multi-Phase Technologies LLC, Geostudi Astier srl) based on tetrahedral finite element modelling (FEM) was used for data inversion. Tetrahedral discretization was used in both forward and inverse modelling. The foreground region was discretized using an ≈0.74-m element size along x and y, i.e. half the average electrode spacing and an ≈0.07-m element size along the z-direction to give the model higher accuracy. This created a 3D resistivity grid, 11 m x 8 m x ≈2 m in size. The background region was discretized using an increasing element size towards the outside of the domain, according to the sequence: 1×, 1×, 2×, 4× and 8× the foreground element size.

Forward modelling was performed using mixed boundary conditions (Dirichlet-Neumann) and a tolerance (stop criterion)

of 1.0 × 10^{-7} for a symmetrical successive over-relaxation conjugate gradient (SSORCG) iterative solver. Data inversion was based on a least squares smoothness constrained approach (LaBrecque et al., 1996). Noise was appropriately managed using a data-weighting algorithm (Morelli and LaBrecque, 1996) that allows the adaptive changes of the variance matrix after each iteration for those data points that are poorly fitted by the model. Inverse modelling was performed using a maximum number of internal inverse preconditioned conjugate gradient (PCG) iterations of 5 and a tolerance (stop criterion) for inverse PCG iterations of 0.001. The amount of roughness from one iteration to the next was controlled to assess maximum layering: a low value of reweight constant (0.1) was set with the objective of generating maximum heterogeneity.

The inverse resistivity models (i.e. models with true resistivity rather than apparent or raw resistivity) were obtained by inverting the datasets acquired through single arrays, or by merging and jointly inverting datasets from different arrays which can deliver better detectability and imaging and, hence, provide more accurate inverse models (Szalai et al., 2009; Torrese, 2020) and more reliable ERT imaging (Seaton and Burbey, 2002; de la Vega et al., 2003). Inversion involved the application of homogeneous starting models that set the average measured apparent resistivity value at each node.
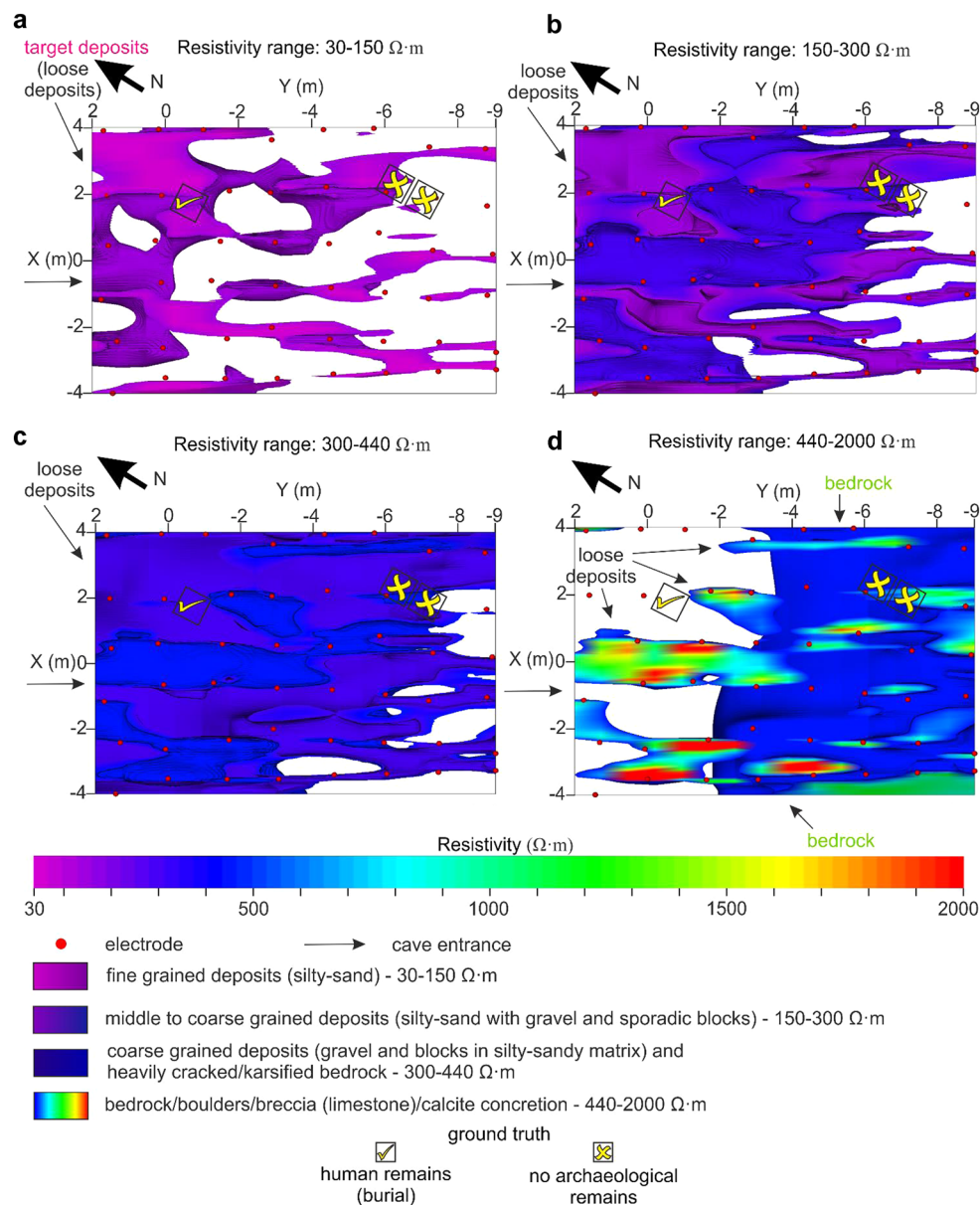
Figure 5. Plan view of different resistivity range extractions from the 3D inverse resistivity model along with lithological description. [Color figure can be viewed at wileyonlinelibrary.com]

The final inverse resistivity models were chosen based on the minimum data residual (or misfit error).

Details on the misfit of inverted data are provided in Supporting Information Table S2.

Bulk total porosity estimation

A realistic, albeit presumed and rough (in the absence of specific measurements), estimate of the bulk total porosity $\varnothing$ for the different resistivity units revealed by ERT was obtained by applying the empirical relationship proposed by Archie (1942):

$$C_t = \frac{1}{a} C_w \varnothing^m S_w^n \tag{1}$$

where C_t is the electrical conductivity of the fluid-impregnated deposit/rock, a is the tortuosity factor, C_w is the electrical conductivity of the fluid impregnating the deposit/rock, $\varnothing$ is the total porosity of the deposit/rock, m is the cementation exponent of the deposit/rock, S_w is the fluid saturation and n is the saturation exponent.

The tortuosity factor a, dimensionless, is related to the path length of the current flow and is used to correct for variation in compaction, pore structure and grain size. Its value typically ranges between 0.5 and 1.5. The cementation exponent m, dimensionless, indicates reduction in the number and size of pore openings. It is affected by lithology, porosity, degrees of compaction and cementation, and age. Its value typically ranges between 1.3 and 2.35 (Salem and Chilingarian, 1999). These factors can be obtained from core analysis. A log–log plot of total porosity $\varnothing$ versus formation factor (Archie, 1942) is used to determine a and m: the tortuosity factor a is the intercept of the least squares fit straight line of the plotted points where $\varnothing = 1$, while the cementation exponent m is determined from the negative slope of the line (Rezaee et al., 2007).

Archie's law relates the *in situ* electrical conductivity of a porous rock to its total porosity and water saturation. It is a purely empirical law attempting to describe ion flow in clay-free porous rocks, with varying intergranular porosity. Electrical conduction is assumed not to be present within the rock grains or in fluids other than water.
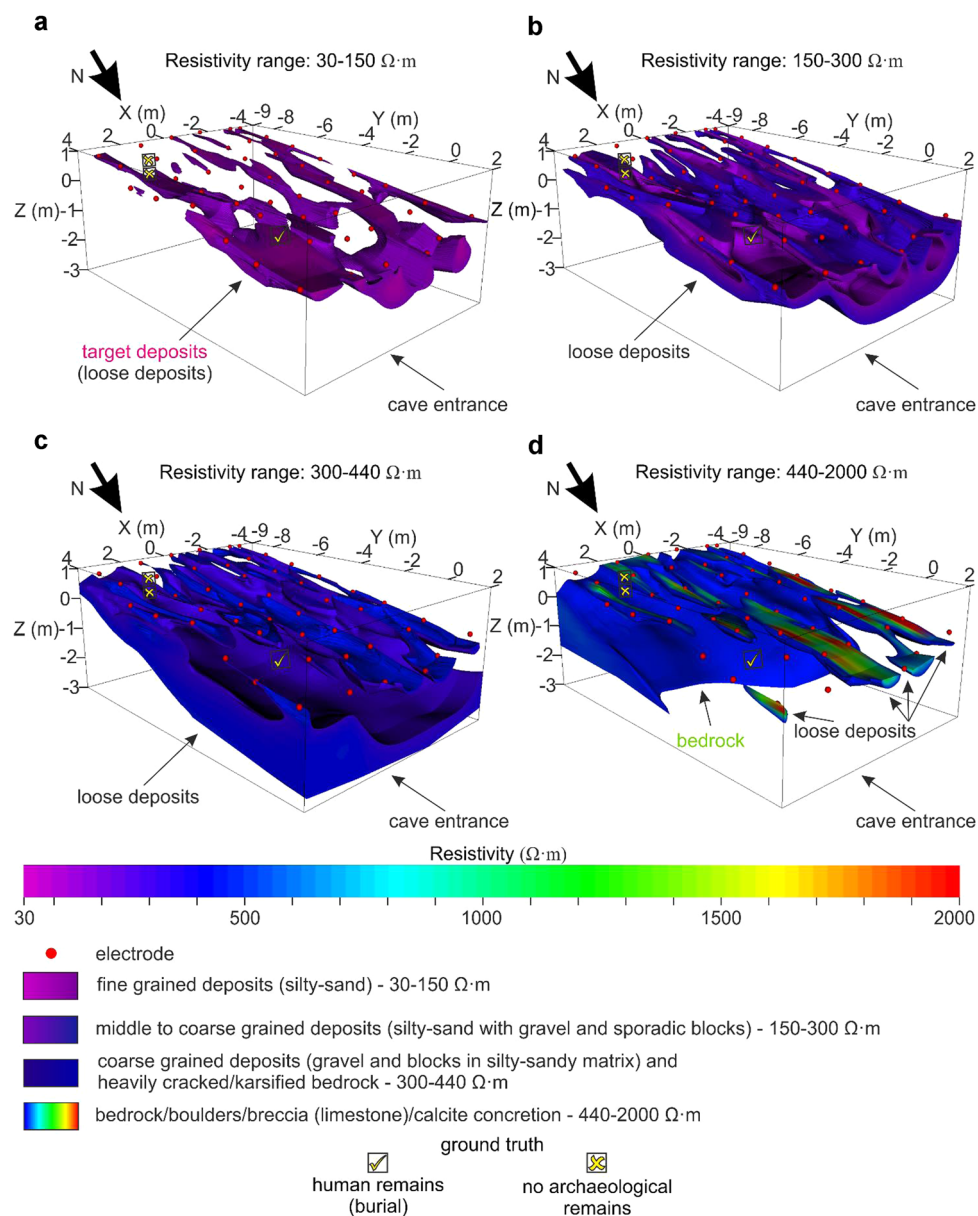
Figure 6. Perspective view from above of different resistivity range extractions from the 3D inverse resistivity model along with lithological description. [Color figure can be viewed at wileyonlinelibrary.com]

Results

Resistivity units

The inverse resistivity results are provided as 3D block models and plane slices extracted from the block models. All models shown here represent merged data obtained from DD, W and WS arrays which delivered better detectability and imaging than single arrays only and therefore provided more accurate inverse models. Data acquired with PsPD arrays were excluded from data merging because the difference in elevation between the remote electrodes installed inside and outside the cave affected their results and therefore they did not provide any imaging improvements.

Misfit in terms of χ^2 errors [330 χ^2 error, 2.6 $\Omega \cdot$ m root mean square (RMS) error for the final iteration; Supporting Information, Table S2] suggests that inverse models are free of artefacts due to an inversion over-fit or excessive smoothing due to an inversion under-fit.

ERT models revealed that resistivity data could be separated into four resistivity units defined based on the expected resistivity values for different lithological units (Figs. 5 and 6): (1) the low-resistivity unit (L) ranging from 30 to 150 $\Omega \cdot$ m is associated with fine-grained deposits (silty-sand); (2) the middle-low resistivity unit (ML) ranging from 150 to 300 $\Omega \cdot$ m is related to fine- to coarse-grained deposits (silty-sand with gravel and sporadic blocks); (3) the middle-high resistivity unit (MH) ranging from 300 to 440 $\Omega \cdot$ m is associated with coarse-grained deposits (gravel and blocks in silty-sandy matrix) and heavily cracked/karst bedrock; and (4) the high resistivity unit (H) ranging from 440 to 2.000 $\Omega \cdot$ m is related to bedrock/boulders/breccia (limestone)/calcite concretions. The measured resistivity values suggest that the geological bodies corresponding to the resistivity units have a low clay content. Only the lowest resistivity deposits (approximately < 100 $\Omega \cdot$ m) included in the low-resistivity unit (30–150 $\Omega \cdot$ m) have some clay content.

The spatial distribution of the different resistivity units related to detrital (loose) deposits shows a longitudinal orientation that follows the primary axis of the cave. The thickness of the archaeological deposits (different types of unconsolidated deposits, such as silty-sand with gravel and sporadic blocks) is highly variable along the primary axis of the cave and ranges from more than 1.5 m at the entrance of the cave to less than 10 cm in the innermost part of the cave where it is discontinuous (Figs. 6–9).
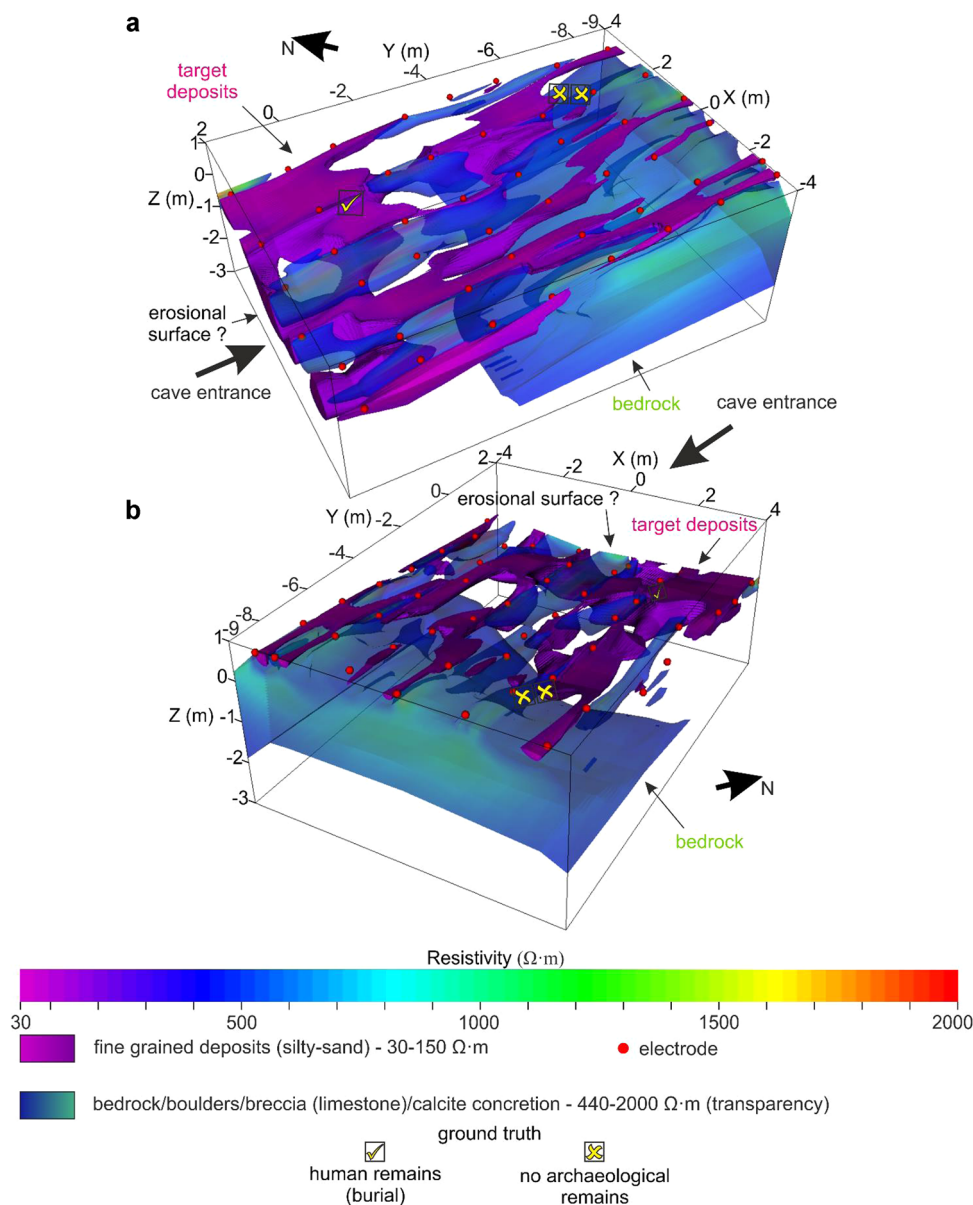
Figure 7. Perspective views from above of different resistivity range extractions from the 3D inverse resistivity model: the low-resistivity unit (the most promising from an archaeological point of view) is highlighted in an opaque plot and the high-resistivity unit in a transparent plot. [Color figure can be viewed at wileyonlinelibrary.com]

Fine-grained deposits (silty-sand) show greater consistency towards the entrance of the cave where they reach a maximum thickness of about 1 m, in the north-east (Figs. 6 and 7).

Transverse to the primary axis of the cave, the bedrock is relatively close to the surface at the south-west and deepens towards the north-east. Obviously, this change affects both the volume and geometry of the overlying archaeological deposits, which follows a gentler slope (Figs. 6–9).

The geometry, thickness and distribution features of the different resistivity units revealed by plan (Fig. 5) and perspective views (Figs. 6–8) are also evident on the cross-section view (Fig. 9). The latter shows x–y plane slices (x, y in Fig. 2) extracted from the 3D block model. Analysis of the cross-sections (Fig. 9) shows that the thickness of the archaeological deposits increases longitudinally towards the entrance of the cave and transversally towards the north-east.

From an archaeological point of view, the low-resistivity unit (30–150 $\Omega \cdot$ m) associated with fine-grained deposits (silty-sand) is the most promising unit; that is, this unit could represent the target deposits. This hypothesis is based on considerations inherent to the electrical resistivity found for

this unit, which indicate the presence of fine-grained deposits that should be easy to excavate.

Bulk total porosity

The estimated bulk total porosity value ∅ ranges between 0.44 and 0.16 for the L unit, 0.16 and 0.13 for the ML unit, 0.13 and 0.1 for the MH unit and is equal to 0.1 for the H unit (Table 1). This estimation, which was based on the application of equation (1), involved:

C_t ranging between 3.3333e-2 and 6.6667e-3 S m^{-1} for the L unit, ranging between 6.6667e-3 and 3.3333e-3 S m^{-1} for the ML unit, ranging between 3.3333e-3 and 2.5e-3 S m^{-1} for the MH unit, and ranging between 2.5e-3 and 5e-4 S m^{-1} for the H unit which are the electrical conductivity values equivalent to the limits of the electrical resistivity range measured for the resistivity units;

a (dimensionless) ranging between 0.5 and 0.7 for the L unit, ranging between 0.7 and 1 for the ML unit, and equal to 1 for the MH and H units;
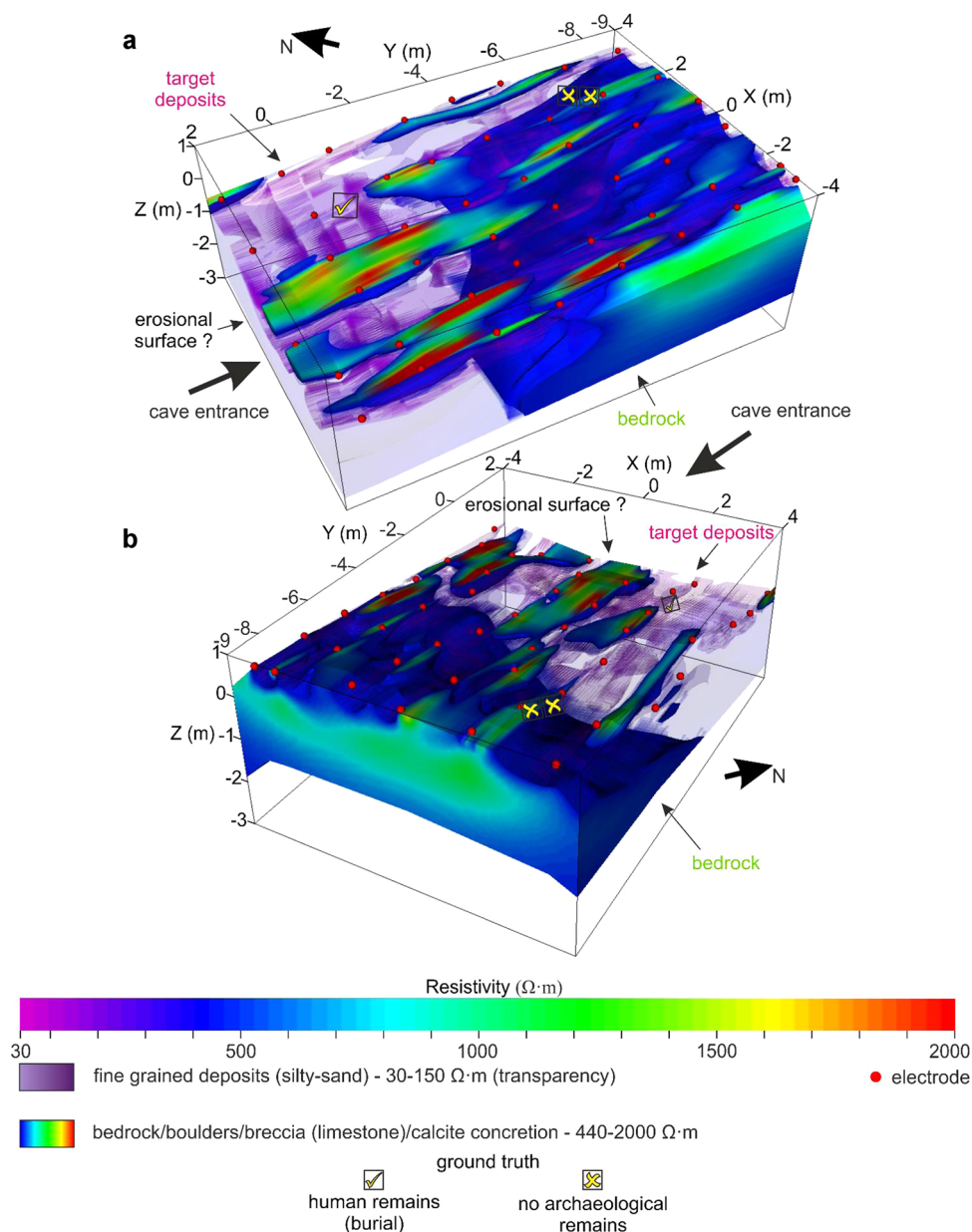
Figure 8. Perspective views from above of different resistivity range extractions from the 3D inverse resistivity model: the high-resistivity unit is highlighted in an opaque plot and the low-resistivity unit (the most promising from an archaeological point of view) in a transparent plot. [Color figure can be viewed at wileyonlinelibrary.com]

$C_w = 0.1\,\mathrm{S\,m^{-1}}$ which has been assumed as a representative value for the water impregnating the deposit/rock (a low mineralized/total dissolved solids water due to poor water–rock interaction);

m (dimensionless) equal to 1.3 for the L, ML and MH units, and ranging between 1.3 (breccia) and 2 (bedrock) for the H unit;

$S_w = 0.7$ (dimensionless), which has been assumed for not fully water saturated deposit/rock:

$n = 2$ (dimensionless).

Cross-validation of geophysical results with observed stratigraphy

To compare resistivity units with stratigraphic aggregates, stratigraphic limits were plotted on the plane slice α (Fig. 2) extracted from the 3D block model (Figs. 10–14). Slice α lies on the same plane as the stratigraphic section a–b (main trench)

(Fig. 2), which allowed us to correlate the two. Geophysical results are consistent with the stratigraphic section (Fig. 10) in identifying the top stratigraphic aggregates of the cave (Negrino *et al.*, 2018) as revealed from previous archaeological surveys.

The erosional surface distinguishes the D aggregate from the underlying aggregates RB, CSB, Gr and BM, which are well defined by the resistivity model (Figs. 10–13). The D, RB and CSB aggregates correspond to the low-resistivity unit (30–150 Ω·m, fine-grained deposits). The Gr aggregate is between the low- and the middle-low resistivity unit (150–300 Ω·m fine-to coarse-grained deposits) due to the presence of coarser deposits. The BM aggregate corresponds to the middle- to low-resistivity unit (Figs. 10–13).

The D aggregate appears irregular in shape, with a heterogeneous resistivity, affected by some disturbance that disrupted the horizontal stratigraphic sequence, with a sharp, erosional contact with the underlying aggregate. Underlying aggregates appear more regular in shape, their resistivity is more homogeneous and they display a smoother contact with older aggregates.
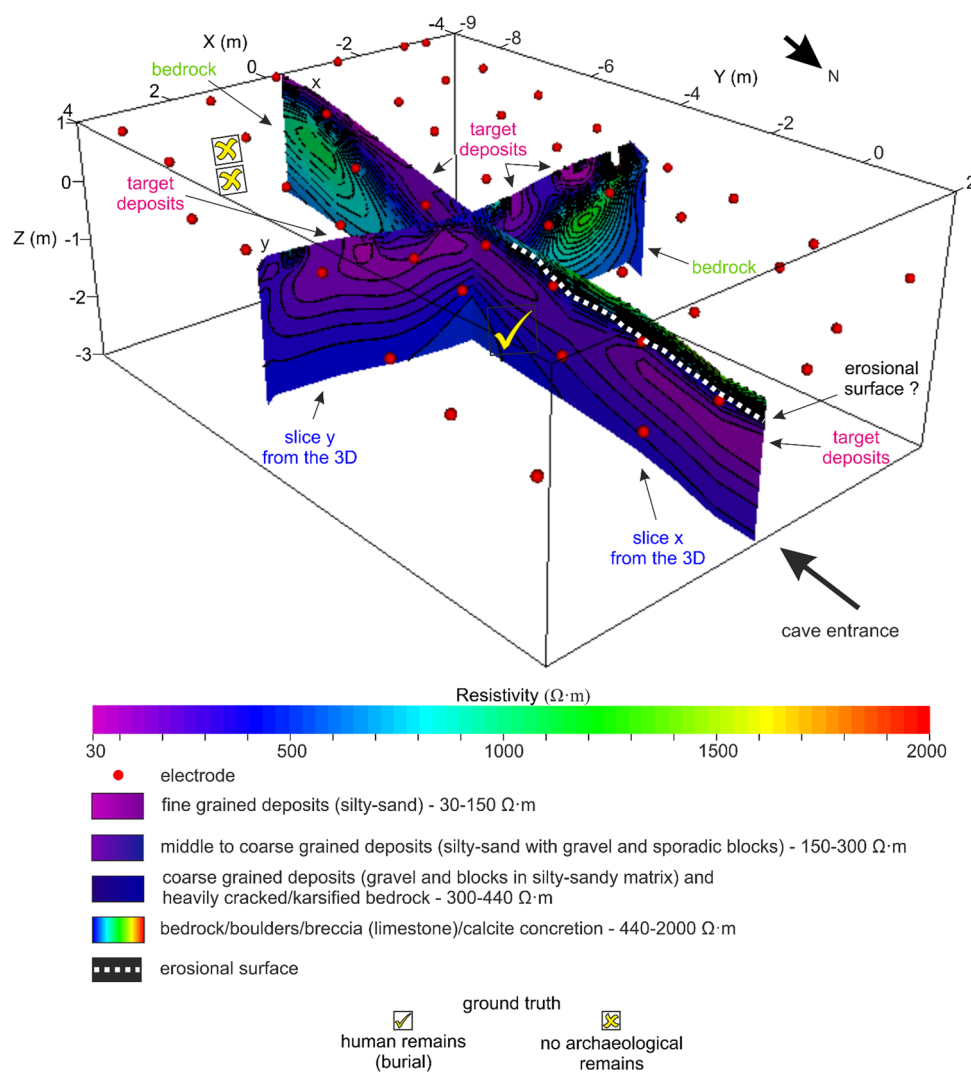
Figure 9. Perspective view of *x*- and *y*-plane slices extracted from the 3D inverse resistivity model showing the resistivity pattern along with lithological descriptions. [Color figure can be viewed at wileyonlinelibrary.com]

The resistivity model fits particular stratigraphy characteristics identified from the sections exposed during excavation, such as:

- the D aggregate dips westward along slice α, but it dips southward along the northern portion of the transverse slice γ. These findings suggest a south-westward dip of the D aggregate (in this restricted area);
- the erosional surface rises slightly in the central part of slice α;
- the RB aggregate dips slightly westward along slice α; it also dips southward along the northern portion of the transverse slice γ. These findings suggest a south-westward dip of the RB aggregate (in this restricted area);
- CSB and Gr aggregates rise slightly in the west part of slice α; they also dip slightly southward along the northern portion of slice γ.

All stratigraphic aggregates show a south-westward dip in the north-east portion of the geophysical model, at the intersection between slices α and γ. Further south, the aggregates appear to fold upwards (Figs. 10–13). In the central part of the geophysical model, the aggregates seem to be slightly bent downwards, as if to form a syncline. This is well defined by the transverse slices x and y (Fig. 9) and the 3D distribution of the low-resistivity unit merged with slices α and γ (Fig. 14).

At a local scale (along the slices), the resistivity pattern shows near continuous and slightly curved units. Some pattern distortion interrupts the continuity of the units. This could be due to the heterogeneity in the grain size distribution within the same stratigraphic aggregate, as shown for the the CSB aggregate (Fig. 10). Conversely, aggregates RB and Gr may show similar resistivity values due to comparable coarse-grained deposit content (Fig. 10).

At the scale of the geophysical model, the resistivity pattern shows a discontinuous distribution of fine-grained (low-resistivity) deposits (Fig. 14) and the recognition of shallow, metre-sized structures with a longitudinal orientation with respect to the primary axis of the cave.

In addition to the erosional surface exposed in excavations of the main trench, the geophysical model also identifies a sharp and irregularly shaped erosional-like surface extending along the primary axis of the cave. This structure is well defined by the resistivity pattern (Figs. 8–10, 14) where it appears as a high-resistivity unit (440–2.000 $\Omega \cdot$ m) as it is filled with mostly coarse deposits.

Cross-validation of geophysical results with observed stratigraphy supports the hypothesis mentioned above that the low-resistivity unit (30–150 $\Omega \cdot$ m), associated with fine-grained deposits (silty-sand), represents the most promising unit from an archaeological point of view. Here, this hypothesis is based on considerations of inherent age and grain size distribution of the corresponding stratigraphic aggregate.

Table 1. Bulk total porosity estimation Ø for the different resistivity units derived from the empirical relationship proposed by Archie (1942), along with the quantities involved in the estimation. The estimate involved the following values: electrical conductivity of the fluid $C_w = 0.1$ S m⁻¹, fluid saturation $S_w = 0.7$, saturation exponent $n = 2$.

	Bulk electrical resistivity of the deposit/rock ($\Omega \cdot$ m)	Bulk electrical conductivity of the deposit/rock, C_t (S m⁻¹)	Tortuosity factor, a	Cementation exponent of the deposit/rock, m	Bulk total porosity, Ø
Low-resistivity unit (L)	30–150	3.3333×10^{-2} to 6.6667×10^{-3}	0.5–0.7	1.3	0.44–0.16
Middle- to low-resistivity unit (ML)	150–300	6.6667×10^{-3} to 3.3333×10^{-3}	0.7–1	1.3	0.16–0.13
Middle- to high-resistivity unit (MH)	300–440	3.3333×10^{-3} to 2.5×10^{-3}	1	1.3	0.13–0.1
High-resistivity unit (H)	440–2.000	2.5×10^{-3} to 5×10^{-4}	1	1.3–2	0.1

Cross-validation of geophysical results with archaeological findings

The archaeological evidence collected during previous field seasons drove the hypothesis that low-resistivity units are the most promising deposits from an archaeological point of view. This can be further tested by determining if the low-resistivity units identified by this study actually correspond to the deposits where archaeological remains have been found. The discovery of a human burial in 2017 provides a good case study to test this, as part of the burial pit was still covered at the time of the geophysical survey. The Early Mesolithic burial, its accompanying grave goods and Epigravettian artefacts located nearby were found in excavation square 2N1E (Fig. 2), which is located near the main trench, towards the entrance of the cave, at the north-east portion of the geophysical survey. These archaeological remains were found within the low-resistivity unit, which is composed mostly of fine-grained deposits (silty-sand) (Fig. 5a). The geophysical survey also shows that the burial was located in the part of the cave with the deepest fine-grained deposits (Figs. 6 and 7). These geophysical findings are consistent with stratigraphic observations from the main trench.

Conversely, no archaeological remains were found in excavation squares -3N4E and -2N4E (Fig. 2), which are located far from the cave entrance, in the south–east portion of the geophysical survey. Interestingly, the low-resistivity unit does not outcrop here or outcrops with negligible thicknesses (Figs. 6 and 7). Geophysical results of those squares suggest the presence of the middle- to low-resistivity unit (Fig. 5b) and a partially middle- to high-resistivity unit (Fig. 5c), which are composed of fine- to coarse-grained deposits (silty-sand with gravel and sporadic blocks) and coarse-grained deposits (gravel and blocks in a silty-sandy matrix), respectively.

The correlation between low-resistivity units and archaeological remains discussed here supports further the hypothesis that the low-resistivity unit (30–150 $\Omega \cdot$ m) associated with fine-grained deposits (silty-sand) represents the most promising unit from an archaeological point of view.

Discussion

The subsurface electrical resistivity pattern allowed us to define the geometry, thickness and sediment distribution of the explorable deposits (Fig. 6), and to map the morphology of the bedrock (Fig. 7). The recognition of variable thicknesses of the loose deposits following the primary axis of the cave and increasing towards the entrance is consistent with field observations. A change in the thickness of the loose deposits has also been observed transversally from the primary axis of the cave, where the thicker part is found in the north-east portion. These findings suggest that the most significant volumes in terms of archaeological excavation are found towards the entrance of the cave on the north-east side.

Cross-validation of geophysical results with the observed stratigraphy revealed that the stratigraphic aggregates are well defined by the resistivity model. Although the resistivity pattern shows near continuous and slightly curved units with some pattern distortion interrupting the continuity of the units at a local scale, it shows a discontinuous distribution of fine-grained (low-resistivity) deposits and the recognition of shallow, metre-sized structures with a longitudinal orientation with respect to the primary axis of the cave at the larger scale. The presence of pattern distortions within individual units could be due to heterogeneity in the grain size distribution.

The geophysical model also allowed the recognition of a possible sharp and irregularly shaped erosional-like surface,
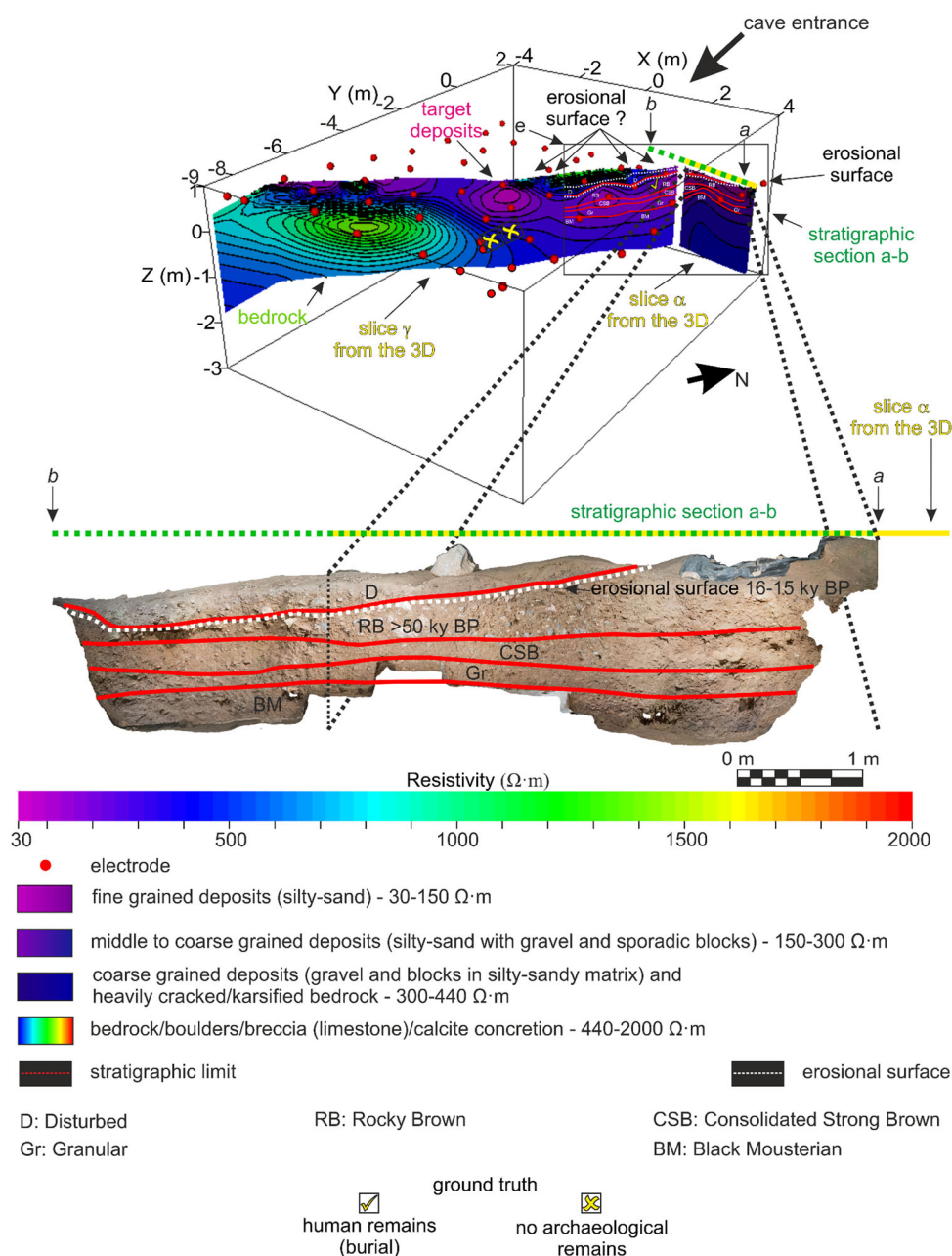
Figure 10. Perspective view of α and γ plane slices extracted from the 3D inverse resistivity model along with the stratigraphic section a–b (main trench): the limits of the stratigraphic aggregates were plotted on slice α which lies on the same plane as the stratigraphic sections a–b, to verify any correlation with the resistivity pattern and extrapolate the stratigraphic limits on slice γ. [Color figure can be viewed at wileyonlinelibrary.com]

filled with mostly coarse deposits, which extends along the primary axis of the cave.

Cross-validation of geophysical results with the archaeological evidence collected during previous field seasons suggests that deposits associated with the low-resistivity unit, i.e. fine-grained deposits (silty-sand), are the most archaeologically promising (Figs. 5–7, 14). Although potential archaeological materials are likely to be found everywhere, fine-grained deposits are easier to dig. Therefore, these deposits might have been favoured by humans when burying their dead. Therefore, we believe that the low-resistivity unit has the highest potential to contain human remains. Geophysical results thus suggest that future archaeological excavations targeting potential burials focus on the low-resistivity unit (Fig. 15), especially on the north-eastern side of the cave where this unit has greater thicknesses (Figs. 6 and 7). It is worth underlining that the middle- to low-resistivity unit, i.e. fine- to coarse-grained deposits (silty-sand with gravel and sporadic blocks) (Figs. 5

and 6), also includes promising deposits as revealed by the rich Mousterian layer exposed by the excavations. In addition, as the geophysical survey did not extend to all portions of the cave, the presence of archaeological remains on the north-western side of the cave, near the entrance of the cave, cannot be excluded.

ERT proved to be an effective technique to define the geometry, thickness, volume and distribution of sediments infilling the cave, and to recognize potential archaeologically interesting structures, specifically shallow, metre-sized, fine-grained structures or pit fill-like structures (e.g. in the burial area, 'human remains' in Fig. 5a). These are crucial data for designing future archaeological field surveys at Arma Veirana cave.

In this strongly heterogeneous geological setting, ERT provided an accurate model, because the electric field tends to flow mainly inside loose, in-cave deposits, which are of low resistivity, rather than flowing through high-resistivity host rocks. Our resistivity model may also have benefited from the
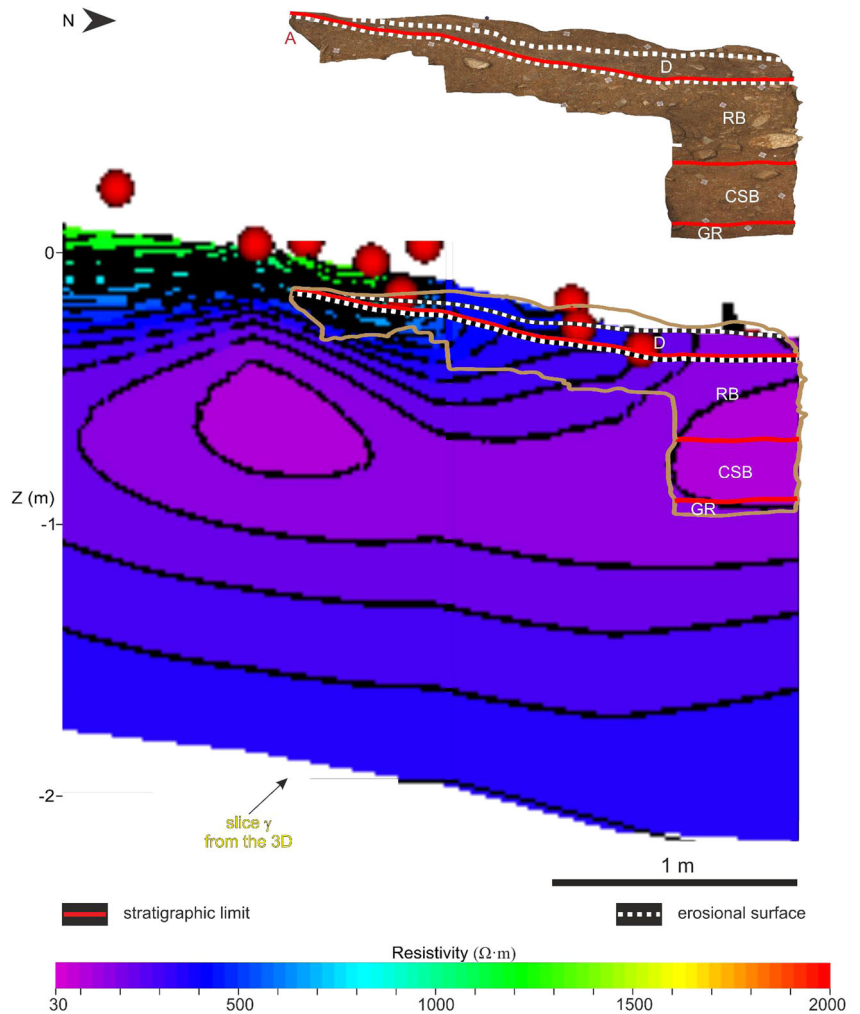
Figure 11. Portion of the γ plane slice extracted from the 3D inverse resistivity model along with photograph and stratigraphic drawing of a portion of the N–S profile: the limits of the stratigraphic aggregates were plotted on slice γ to verify any correlation with the resistivity pattern. [Color figure can be viewed at wileyonlinelibrary.com]

3D cave geometry. At the middle of the surveyed area, the average thickness of sediments is 1.33 m and the cave's half-width at floor level is 4.48 m; moreover, the cave has downward diverging walls. This is consistent with findings from Olenchenko *et al.* (2020) who suggested that accurate resistivity models can be obtained by ERT inside a cave whose half-width is larger than the thickness of sediments and in the case of downward diverging cave walls.

This study also showed that the main drawback of the ERT method is that the properties of heterogeneous cave deposits can be characterized by a wide range of possible resistivity values depending on the heterogeneity in the grain size distribution (e.g. Schrott and Sass, 2008), as well as by actual physical and chemical states of the deposits. Furthermore, as some of these parameters are environmentally dependent (e.g. water saturation conditions), a homogeneous stratigraphic aggregate may also show resistivity variations. Therefore, the resistivity measured in this study can vary even within the same stratigraphic aggregate or be similar for different stratigraphic aggregates. In this sense, it is worth underlining that aggregates RB and Gr may show similar resistivity values due to similar coarse-grained deposit content; conversely, the CSB aggregate appears to be affected by some disturbance that disrupts its horizontal continuity even if it is locally strongly heterogeneous. This eventuality is clearly shown by slices α and γ that have been cross-validated with stratigraphic observations.

Regarding the application of equation (1) for the bulk total porosity estimation, although the applicability of Archie's law may be argued and is questionable for the investigated in-cave deposits, its adoption is motivated by the evidence that these materials are affected by a negligible clay content. Only the lowest resistivity deposits (approximately < 100 $\Omega \cdot m$) included in the low-resistivity unit (30–150 $\Omega \cdot m$) have some clay content. However, clay-related electrical conductivity (Waxman and Smits, 1968) appears to give a negligible contribution to the bulk electrical conductivity of the materials considering that clay is dispersed in the solid matrix of the deposits.

We believe that our resistivity data are not significantly influenced by heavy mineral composition in the sediments. Although cave sediments may represent low oxygen and chemically reducing environments, evidence of manganese oxides was found only in the BM aggregate at the base of the currently exposed stratigraphy. Field and micromorphological analyses do not indicate extensive reducing conditions in the deposits. We do not have any evidence of the manganese origin associated with a past inner-cave reducing environment; by contrast, the BM aggregate with its anthropic content suggests that the manganese origin may be associated with soil humification after the human occupation of Veirana cave.

As a result of anthropogenic activities, a high content of organic matter was deposited and decomposed in the typical environmental conditions of the cave vestibule, where darkness and humidity promoted the growth of saprophyte microorganisms that led to the decomposition and mineralization of organic matter, in turn generating humic acids and chelate coordination complexes, which increased metal solubility and mobility (Marìn Arroyo *et al.*, 2008).
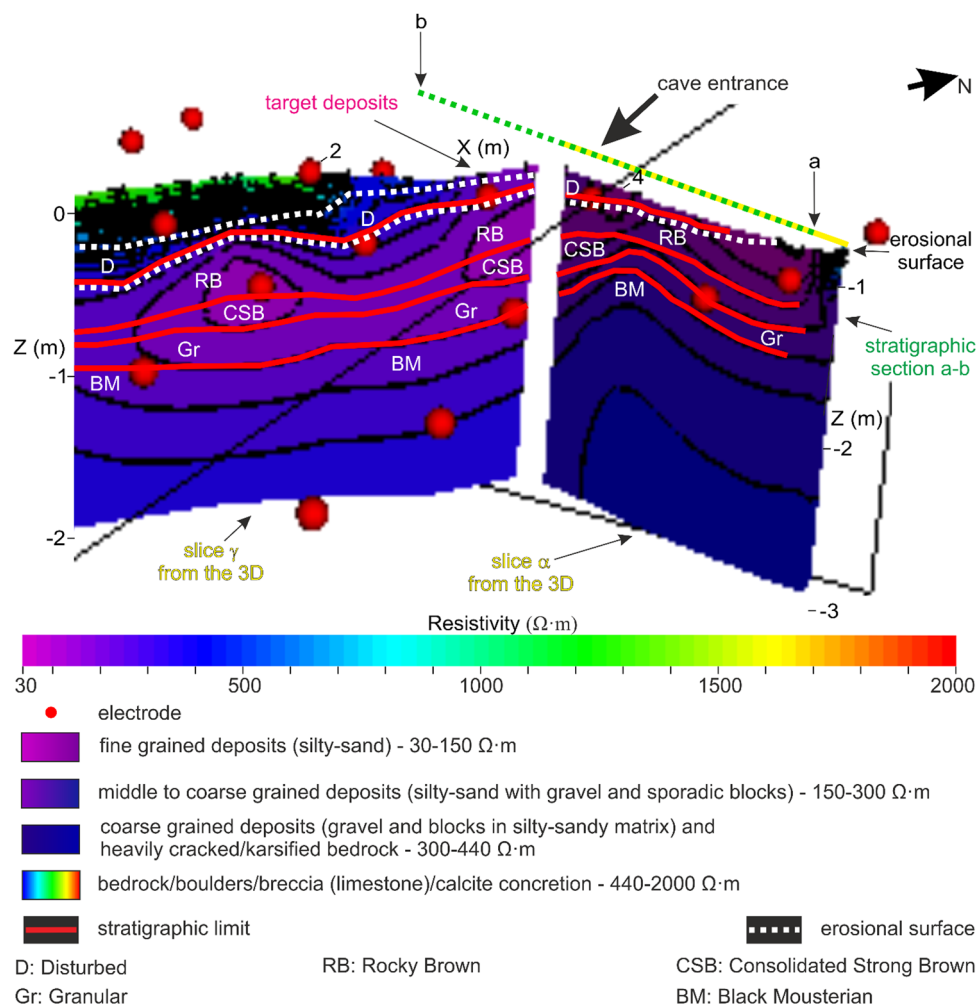
Figure 12. Enlargement of the e portion of Fig. 10: perspective view of α and (partly) γ plane slices extracted from the 3D inverse resistivity model along with stratigraphic limits derived from the stratigraphic section a–b (main trench): the limits between the stratigraphic aggregates were plotted on slice α, which lies on the same plane as the stratigraphic section a–b, to verify any correlation with the resistivity pattern and extrapolate the stratigraphic limits on slice γ. [Color figure can be viewed at wileyonlinelibrary.com]

Due to these conditions, the evolution of the sediment itself and carbonate percolation from the surrounding rocks (the Val Tanarello limestones and the dolomitic breccia) slowed humification of the sediments, thus increasing the pH and causing manganese precipitation in the form of oxides and hydroxides (Hill, 1982). The origin of the manganese in the BM layer may therefore be due to the degradation of its organic materials and to its later evolution as a buried anthropic sediment inside a carbonatic system subject to percolation.

Speleogenesis model of Arma Veirana cave

Reiterating that the study of the cave and its valley are at an early stage, the data collected in the last few years of field surveys allow us to offer an early interpretation of its genesis and evolution.

The first consideration deals with the stratigraphy of the rock in which the cave opens and the cave mesoscale morphology: the proto-Veirana fold generated into a sedimentary sequence that runs from Late Jurassic (the Kimmeridgian–Berriasian Val Tanarello limestone) to Eocene (the 'late Cretaceous–middle Palaeogene' rocks of the Caprauna Formation).

Above the Val Tanarello limestone, we find a tectonic contact with a dolomitic breccia referred to as the 'Brecce Dolomitiche Vacuolari' of Scitic–Anisic age; down from the Veirana entrance and from the Costa Losera flank, the evolution of the Neva valley cut away all proximal carbonatic

formations, which directed the Rio Neva flow to an impermeable substratum, the formation of the 'Quarziti di Ponte di Nava' of the Lopingian/Lower Triassic: the contact between the 'Caprauna Formation' and the physically lower 'Quarziti di Ponte di Nava' is also tectonic.

Therefore, the geology of the area is very complex both regarding its tectonic setting and its geomorphological evolution (Seno et al., 2003), but for the present study, it is important to note that the sequence of the basement fold is inverted and that the ceiling and the lateral walls of the Veirana, located inside the fold, are related to the folded strata of the 'Val Tanarello limestone', locally covered by secondary carbonate depositions of the cave.

At first glance, we cannot see clear evidence of strata related to the 'Caprauna Formation' inside the cave itself, which suggests that the empty space of the cave replaced the missing strata. The flanks of the fold at the cave entrance confirm this idea, as this is where we find schists of the 'Caprauna Formation' in their correct stratigraphic position and with the appropriate parasitic folds.

The lack of strata of the 'Caprauna Formation' inside the cave needs explaining, as it is the reason why the cave was formed. When thinking about the genesis of karst systems, it is easy to embrace the paradigm of karstification by 'total removal', where carbonate caves are the result of a chemical dissolution – i.e. the physical transition of solid-state compounds into a liquid phase where both the residual
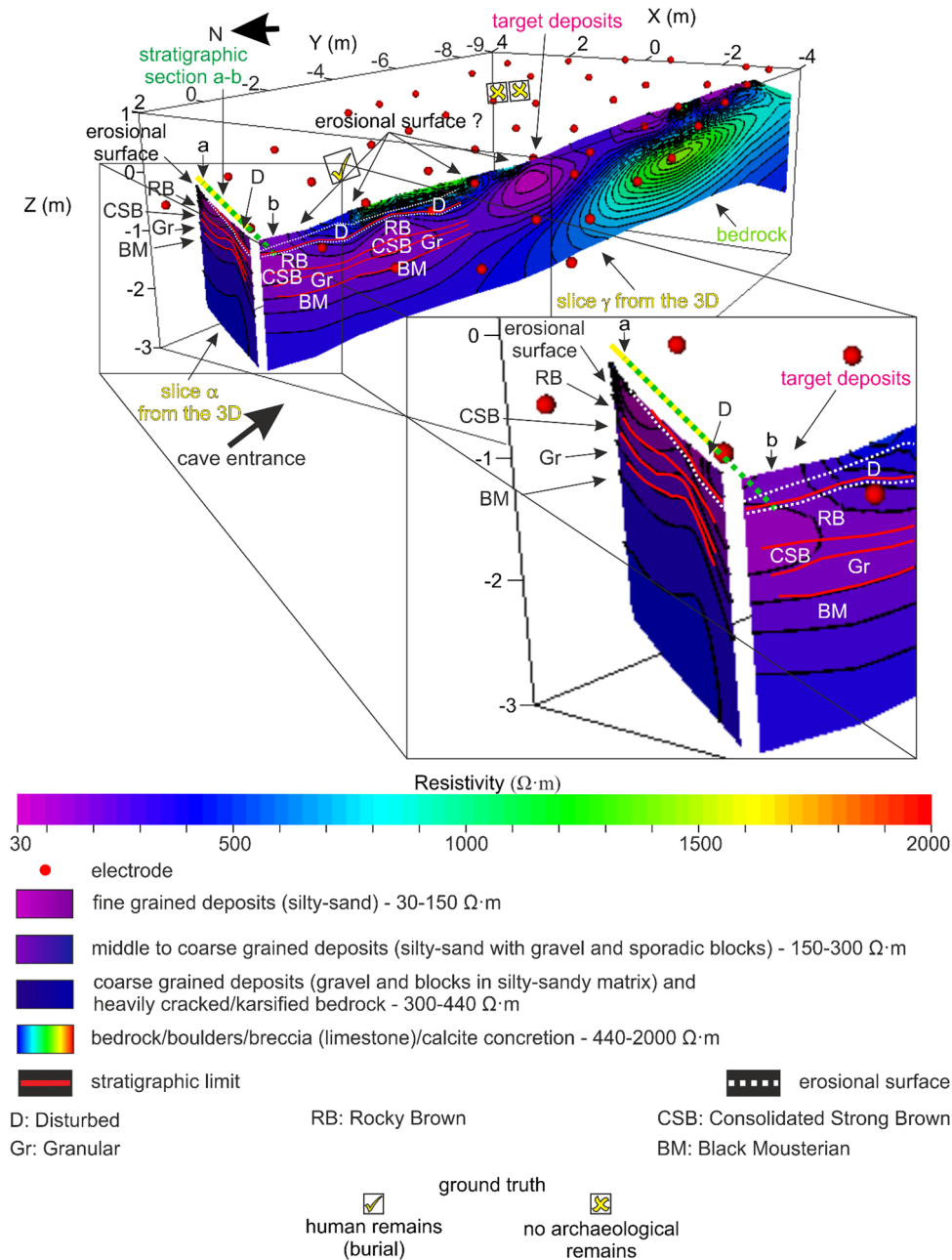
Figure 13. Perspective view of α and γ plane slices extracted from the 3D inverse resistivity model along with the stratigraphic section a–b (main trench): the limits of the stratigraphic aggregates were plotted on slice α which lies on the same plane as the stratigraphic section a–b, to verify any correlation with the resistivity pattern and extrapolate the stratigraphic limits on slice γ. [Color figure can be viewed at wileyonlinelibrary.com]

insoluble deposit and the dissolved elements are then carried away by water flow. However, this is not the case of the Arma Veirana, as it never had a cave river system. Therefore, we cannot refer to the cave as a 'karst system' or even part of an old one.

The Arma Veirana is a 'void' inside an antiform syncline. The potential energy of the system was near zero before deepening of the rio Neva palaeovalley; therefore, epigenesis could not have produced the cave because the very low water flow rate would not have allowed the undissolved elements to be flushed out of the system. Instead, the initial solid phase was formed by the less competent rock layers that were fractured during the folding because of the high strain concentrated in the hinge region (Cosgrove, 2015). The fractured solid phase was then separated into a liquid phase that removed the soluble ions and colloids through a very low fluid flow, and then into a residual solid phase which remained in place in the form of an alterite: this latter is what we call

'ghost-rock' (Quinif, 2014, 2018). The residual alterite could not exit the system, thus fitting the concept of karstification 'without total removal' (Quinif, 2014).

In a subsequent stage of a cave forming through such a process, the potential energy usually increases due to some geological event such as glacial rebound or eustatic rebound. In the case of the palaeo-Veirana, the potential energy probably grew due to deepening of the Rio Neva palaeovalley: in such a situation, the residual solid phase may have been removed by 'piping' phenomena with the genesis of a suffusion cave stage (Bartolomé et al., 2015).

We are still evaluating the role of the palaeo-Neva in the removal of the 'ghost rock' from the cave: we do not yet have any evidence of an ingression of the rio Neva inside the cave, but it is clearly possible. In addition, the morphological regularity of the bedrock made visible by our geophysical model could be related to an erosion surface generated by water flow during deepening of the valley. In this sense, the
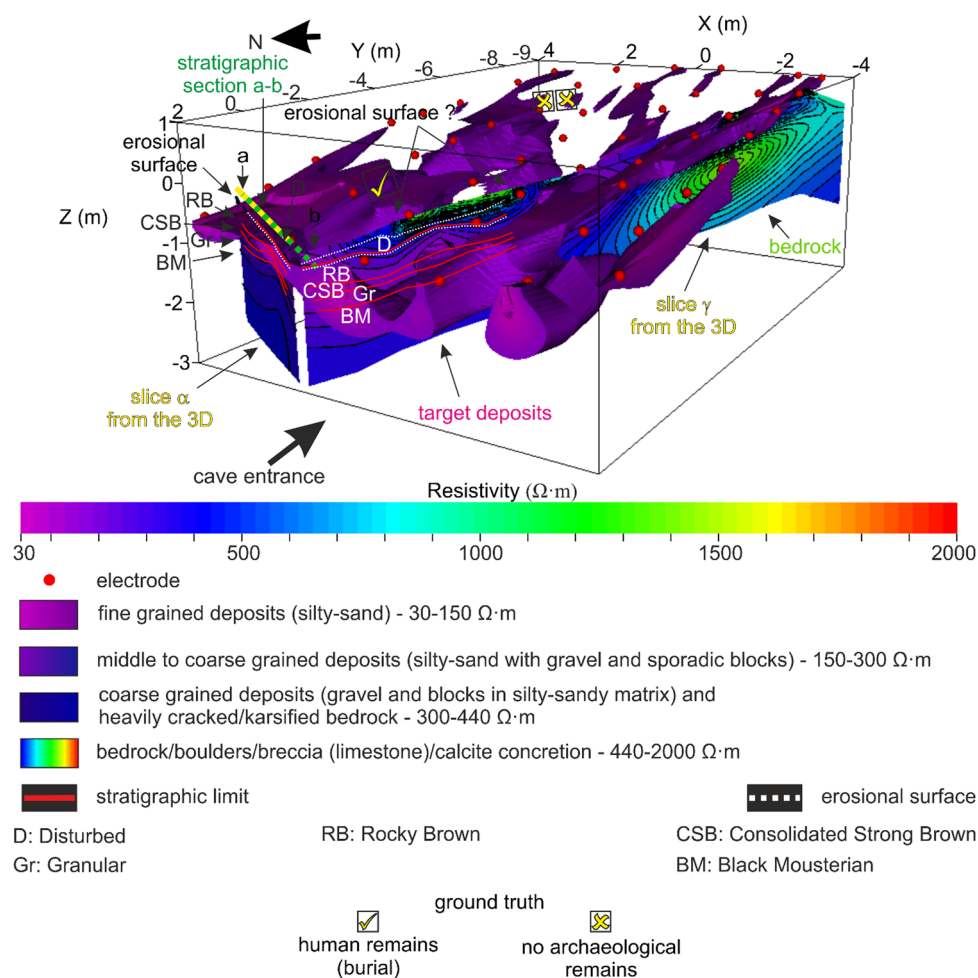
Figure 14. Perspective view of α and γ plane slices extracted from the 3D inverse resistivity model along with the stratigraphic section a–b (main trench): the limits of the stratigraphic aggregates were plotted on slice α which lies on the same plane as the stratigraphic section a–b, to verify any correlation with the resistivity pattern and extrapolate the stratigraphic limits on slice γ; the 3D distribution of the low-resistivity unit, the most promising from an archaeological point of view, has been also plotted for comparison. [Color figure can be viewed at wileyonlinelibrary.com]

gully-like morphology that we see in our geophysical model is of particular significance if we assume that the surviving vertical strata of different competence, at the bottom of the cave, were subjected to an erosional water sheet flow inside the open fold after the pseudokarst genetic stages previously suggested. Similar situations have been described in other caves of this kind, such as the Ladies Cave Anticline at Sandersfoot (Pembrokeshire, UK), the Cave of Harpea (Basque Country, Pyrenees) and the Anticline Cave at Wellington (Australia): the last is a hypogene multiphase cave (Osborne, 2010). However, to confirm and clarify the hypothesized ideas presented here, more field studies are needed. In particular, we plan on creating a geological trench far from the archeological deposits, which will uncover the 'bedrock', thus allowing us to evaluate its geological characteristics more precisely.

Conclusions

We have presented 3D ERT imaging of the archaeological deposits at Arma Veirana cave (northern Italy), to date only partially explored during a series of four archaeological field seasons.

We obtained a subsurface electrical resistivity pattern with the main aims to define the geometry, thickness and sediment distribution features of the deposits, and map the morphology of the underlying bedrock. This study revealed that the

thickness of the deposits is variable along the primary axis of the cave and ranges between more than 1.5 m towards the entrance of the cave to less than 10 cm towards its innermost part, where the deposits show a discontinuous distribution. A change in the thickness of the deposits has also been revealed transverse to the primary axis of the cave, with a thickening towards the north-east side. The study allowed the recognition of shallow, metre-sized, fine-grained sediment-filled structures with a longitudinal orientation with respect to the primary axis of the cave, as well as a possible erosional-like structure, filled with mostly coarse deposits, which extends along the primary axis of the cave.

The results of the geophysical survey were cross-validated with the exposed stratigraphy as well as with the presence of archaeological material culture. Both supported the hypothesis that the low-resistivity unit, which includes fine-grained structures, is the most archaeologically promising. The results also suggest that the middle- to low-resistivity unit can also be linked to rich archaeological layers.

These results will be useful to design future archaeological surveys at Arma Veirana cave and they provide further insights on the applicability and effectiveness of 3D ERT in investigating any in-cave deposits. Although ERT has rarely been employed in Palaeolithic cave contexts because Palaeolithic remains are typically disseminated in loose deposits and either do not possess high electrical resistivity contrasts or are too small to be detected, an accurate resistivity model was obtained in this study. Even though this model did not
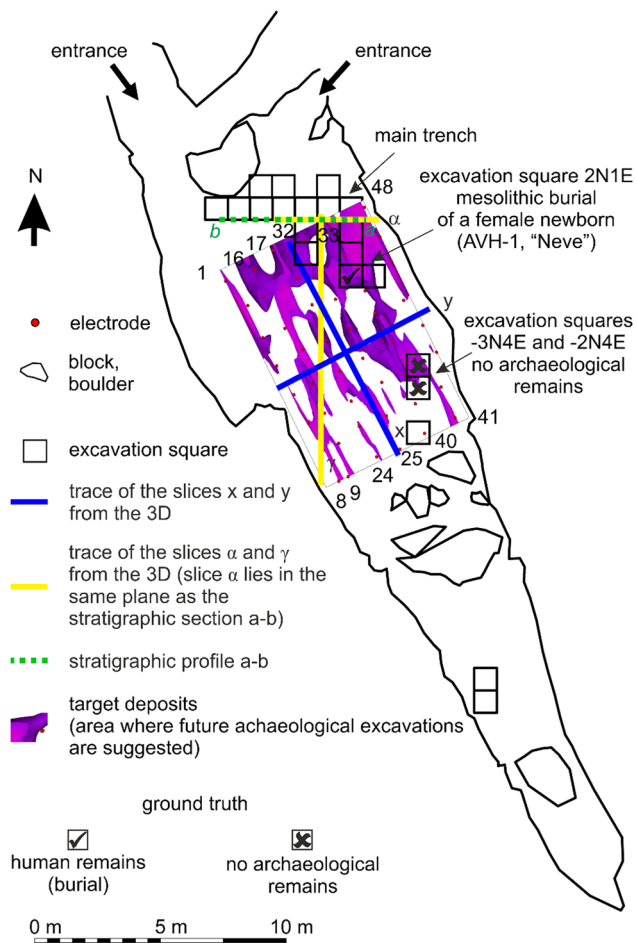
Figure 15. Plan distribution of the low-resistivity unit (30–150 Ω·m, fine-grained deposits), the most promising from an archaeological point of view, along with the experimental layout of the ERT survey. [Color figure can be viewed at wileyonlinelibrary.com]

recognize any specific remains, it defined the properties and volume of the explorable deposits and identified the most promising areas to excavate, i.e. probable artefact-bearing deposits.

As regards the issues derived from the application of ERT in such a confined cave environment, the results of our study are consistent with previous findings that accurate resistivity models can be obtained by ERT inside a cave whose half-width is larger than the thickness of sediments and in the case of downward diverging cave walls.

Supplementary data

The data used in this study are available on Zenodo, https://doi.org/10.5281/zenodo.4544550, (Torrese et al., 2021b).

Supporting information

Additional supporting information can be found in the online version of this article. This article includes online-only Supplemental Data.

Text S1. Excavation, laboratory methods and documentation.
Table S1. Quality of resistivity raw data.
Table S2. Misfit of inverted resistivity data.
Figure S1. Photographs from main trench (stratigraphic section a–b, E–W profile, Fig. 2), lithological description of the aggregates and associated images.

References

Abu Zeid N, Bignardi S, Russo P *et al.* 2019. Deep in a Paleolithic archive: integrated geophysical investigations and laser-scanner reconstruction at Fumane Cave, Italy. *Journal of Archaeological Science: Reports* **27**: 101976.

Al-Zoubi AS, Abueladas AEA, Al-Rzouq RI *et al.* 2007. Use of 2D Multi Electrodes Resistivity Imagining for Sinkholes Hazard Assessment along the Eastern Part of the Dead Sea, Jordan. *American Journal of Environmental Sciences* **3**: 230–234. https://doi.org/10.3844/ajessp.2007.230.234

Archie GE. 1942. The electrical resistivity log as an aid in determining some reservoir characteristics. *Transactions of the AIME* **146**: 54–62. https://doi.org/10.2118/942054-G

Astin T, Eckardt H, Hay S. 2007. Resistivity imaging survey of the Roman Barrows at Bartlow, Cambridgeshire, UK. *Archaeological Prospection* **14**: 24–37. https://doi.org/10.1002/arp.287

Bartolomé M, Sancho C, Moreno A *et al.* 2015. Upper Pleistocene interstratal piping-cave speleogenesis: the Seso Cave System (Central Pyrenees, Northern Spain). *Geomorphology* **228**: 335–344. https://doi.org/10.1016/j.geomorph.2014.09.007

Beck A, Weinstein-Evron M. 1997. A geophysical survey in the el-Wad cave, Mount Carmel, Israel. *Archaeological Prospection* **4**: 85–91.

Becker RJ, Janković I, Ahern JCM *et al.* 2019. High data density electrical resistivity tomography survey for sediment depth estimation at the Romuald's Cave site. *Archaeological Prospection* **26**: 361–367. https://doi.org/10.1002/arp.1749

Berge MA, Drahor MG. 2011a. Electrical resistivity tomography investigations of multilayered archaeological settlements: Part I – modelling. *Archaeological Prospection* **18**: 159–171.

Berge MA, Drahor MG. 2011b. Electrical resistivity tomography investigations of multilayered archaeological settlements: Part II - a case from Old Smyrna Höyük, Turkey. *Archaeological Prospection* **18**: 291–302. https://doi.org/10.1002/arp.423

Bertok C, Martire L, Perotti E *et al.* 2011. Middle-Late Jurassic syndepositional tectonics recorded in the Ligurian Briançonnais succession (Marguareis–Mongioie area, Ligurian Alps, NW Italy). *Swiss Journal of Geosciences* **104**: 237–255. https://doi.org/10.1007/s00015-011-0058-0

Bronk Ramsey CB. 2009. Bayesian analysis of radiocarbon dates. *Radiocarbon* **51**: 337–360. https://doi.org/10.1017/S0033822200033865

Campana S, Piro S. 2008. *Seeing the Unseen. Geophysics and Landscape Archaeology.* 1st edn. CRC Press: Boca Raton.

Cardarelli E, Di Filippo G, Tuccinardi E. 2006. Electrical resistivity tomography to detect buried cavities in Rome: a case study. *Near*

Surface Geophysics 4: 387–392. https://doi.org/10.3997/1873-0604.2006012

Carrière SD, Chalikakis K, Sénéchal G et al. 2013. Combining Electrical Resistivity Tomography and Ground Penetrating Radar to study geological structuring of karst Unsaturated Zone. Journal of Applied Geophysics 94: 31–41.

Cosgrove JW. 2015. The association of folds and fractures and the link between folding, fracturing and fluid flow during the evolution of a fold-thrust belt: a brief review. In Industrial Structural Geology: Principles, Techniques and Integration, Richards FL, Richardson NJ, Rippington SJ, Wilson RW, Bond CE (eds). Geological Society: London.

Cozzolino M, Caliò LM, Gentile V et al. 2020. The discovery of the Theater of Akragas (Valley of Temples, Agrigento, Italy): an archaeological confirmation of the supposed buried structures from a geophysical survey. Geosciences 10: 161.

Dahlin T, Loke MH. 1998. Resolution of 2D Wenner resistivity imaging as assessed by numerical modelling. Journal of Applied Geophysics 38: 237–249.

Dal Bo G, Laiolo G, Lazzarini G. 1978. L'Arma di Costa di Cerisola. Stalattiti e stalagmiti – Gruppo Speleologico Savonese 16: 14 (in Italian).

Dallagiovanna G, Gaggero L, Seno S et al. 2011. Note Illustrative della Carta Geologica d'italia alla scala 1:50.000, foglio 228, Cairo Montenotte. ISPRA – Servizio Geologico d'Italia.

Decarlis A, Lualdi A. 2009. A sequence stratigraphic approach to a Middle Triassic shelf-slope complex of the Ligurian Alps (Ligurian Brianconnais, Monte Carmo-Rialto unit, Italy). Facies 55: article no 267. https://doi.org/10.1007/s10347-008-0170-4

Deiana R, Bonetto J, Mazzariol A. 2018. Integrated electrical resistivity tomography and ground penetrating radar measurements applied to tomb detection. Surveys in Geophysics 39: 1081–1105. https://doi.org/10.1007/s10712-018-9495-x

de la Vega M, Osella A, Lascano E. 2003. Joint inversion of Wenner and dipole-dipole data to study a gasoline-contaminated soil. Journal of Applied Geophysics 54: 97–109. https://doi.org/10.1016/j.jappgeo.2003.08.020

Drahor MG, Berge MA, Kurtulmuş TÖ et al. 2008. Magnetic and electrical resistivity tomography investigations in a Roman legionary camp site (Legio IV Scythica) in Zeugma, southeastern Anatolia, Turkey. Archaeological Prospection 15: 159–186. https://doi.org/10.1002/arp.332

Dubois C, Lans B, Kaufmann O et al. 2011. Karstification de type fantomes de roche en Entre-deux-Mers (Gironde, France): implications en karstogenèse et morphologie karstique. Karstologia: Revue de Karstologie et de Spéléologie Physique 57, 1er semester: 19–27.

El-Qady G, Metwaly M, Drahor MG. 2019. Geophysical techniques applied in archaeology, Archaeogeophysics: State of the Art and Case Studies. Springer: Cham; 1–25.

Fikos I, Vargemezis G, Pennos C et al. 2019. Processing 2D ERT data in 3D environment – A case study inside a karstic cave in Greece. 25th European Meeting of Environmental and Engineering Geophysics Vol. 2019; 1–5.

Goldberg P, Sherwood SC. 2006. Deciphering human prehistory through the geoarcheological study of cave sediments. Evolutionary Anthropology 15: 20–36. https://doi.org/10.1002/evan.20094

Goudie AS. 2013. Encyclopedia of Geomorphology, Vol. I. Routledge: London.

Griffiths DH, Barker RD. 1993. Two-dimensional resistivity imaging and modelling in areas of complex geology. Journal of Applied Geophysics 29: 211–226. https://doi.org/10.1016/0926-9851(93)90005-J

Guerin R, Benderitter Y. 1995. Shallow karst exploration using MT-VLF and DC resistivity method. Geophysical Prospecting 43: 635–653.

Hancock AJ. 1999. An investigation of the soils and sediment contained within the entrance chamber (or The Vestibule), Peak Cavern, and the assessment of their archaeological significance through the integration of geophysical techniques. BSc Project. Department of Archaeological Sciences, University of Bradford.

Hill CA. 1982. Origin of black deposits in caves. National Speleological Society Bulletin 44: 15–19.

Hirniak JN, Smith EI, Johnsen R et al. 2020. Discovery of cryptotephra at Middle–Upper Paleolithic sites Arma Veirana and Riparo

Bombrini, Italy: a new link for broader geographic correlations. Journal of Quaternary Science 35: 199–212. https://doi.org/10.1002/jqs.3158

Hodgkins J, Orr CM, Gravel-Miguel C et al. 2021. An infant burial from Arma Veirana in northwestern Italy provides insights into funerary practices and female personhood in early Mesolithic Europe. Scientific Reports 11: 23735. https://doi.org/10.1038/s41598-021-02804-z

Jol HM, Schroder JF, Reeder P et al. 2002. Return to the Cave of Letters (Israel): a ground penetrating radar archaeological expedition In: Proceedings of the Eighth International Conference on Ground Penetrating Radar (GPR 2000), Noon DA, Stickley GF, Longstaff D (eds). SPIE 4084: 882–886.

Kneisel C. 2006. Assessment of subsurface lithology in mountain environments using 2D resistivity imaging. Geomorphology 80: 32–44. https://doi.org/10.1016/j.geomorph.2005.09.012

LaBrecque DJ, Miletto M, Daily W et al. 1996. The effects of noise on Occam's inversion of resistivity tomography data. Geophysics 61: 538–548. https://doi.org/10.1190/1.1443980

Laigre L, Reynards E, Arnaud-Fassetta G et al. 2012. Characterisation of the Rhône river palaeodynamics in Central Valais (Switzerland) with the electrical resistivity tomography method. Géomorphologie: Relief, Processus, Environnement 4: 405–426.

Loke MH, Acworth I, Dahlin T. 2003. A comparison of smooth and blocky inversion methods in 2D electrical imaging surveys. Exploration Geophysics 34: 182–187.

Loke MH, Barker RD. 1996. Rapid least-squares inversion of apparent resistivity pseudosections by a quasi-Newton method. Geophysical Prospecting 44: 131–152.

Maillol JM, Seguin M-K, Gupta OP et al. 1999. Electrical resistivity tomography survey for delineating uncharted mine galleries in West Bengal, India. Geophysical Prospecting 47: 103–116.

Matias HC, Monteiro Santos FA, Rodrigues, Ferreira FE et al. 2006. Detection of graves using the micro-resistivity method. Annals of Geophysics 49.

Mallol C, Goldberg P. 2017. Caves and rockshelter sediments. In Archaeological Soil and Sediment Micromorphology, Nicosia C, Stoops G (eds). Wiley: Hoboken; 359–377.

Marín Arroyo AB, Landete Ruiz MD, Vidal, Bernabeu G et al. 2008. Archaeological implications of human-derived manganese coatings: a study of blackened bones in El Mirón Cave, Cantabrian Spain. Journal of Archaeological Science 35: 801–813. https://doi.org/10.1016/j.jas.2007.06.007

Morelli G, LaBrecque DJ. 1996. Advences in ERT inverse modeling. European Journal of Environmental and Engineering Geophysics 1: 171–186.

Negrino F, Benazzi S, Hodgkins J et al. 2018. Erli (SV). Arma Veirana. In Archeologia in Liguria, Nuova Serie VI, 2014-2015, Soprintendenza Archeologia, Belle Arti e Paesaggio per la città metropolitana di Genova e le province di Imperia, Savona e la Spezia, Genova, 460–461.

Oberender P, Plan L. 2018. A genetic classification of caves and its application in eastern Austria, Advances in Karst Research: Theory, Fieldwork and Applications. Geological Society: London; 121–136.

Obradovic M, Abu Zeid N, Bignardi S et al. 2015. High resolution geophysical and topographical surveys for the characterisation of Fumane Cave prehistoric site, Italy: Near Surface Geoscience 2015. 21st European Meeting of Environmental and Engineering Geophysics.

Olenchenko V, Tsibizov L, Osipova P. 2019. Electrotomography in a cave: a numerical experiment. Interexpo GEO-Siberia 2: 111–115. https://doi.org/10.33764/2618-981X-2019-2-2-111-115

Olenchenko VV, Tsibizov LV, Osipova PS et al. 2020. Peculiarities of using 2D electrical resistivity tomography in caves. Archaeology, Ethnology and Anthropology of Eurasia 48: 67–74. https://doi.org/10.17746/1563-0110.2020.48.4.067-074

Ortega AI, Benito-Calvo A, Porres J et al. 2010. Applying electrical resistivity tomography to the identification of endokarstic geometries in the Pleistocene Sites of the Sierra de Atapuerca (Burgos, Spain). Archaeological Prospection 17: 233–245. https://doi.org/10.1002/arp.392

Osborne RAL. 2010. Rethinking eastern Australian caves. Geological Society, London, Special Publications 346: 289–308. https://doi.org/10.1144/SP346.15

Osipova PS, Olenchenko VV, Tsibizov LV et al. 2020. The study of Paleolithic monuments in karst caves by electrotomography. *Engineering and Mining Geophysics* **2020**: 1–8.

Papadopoulos NG, Sarris A, Parkinson WA et al. 2014. Electrical resistivity tomography for the modelling of cultural deposits and geomophological landscapes at Neolithic sites: a case study from Southeastern Hungary. *Archaeological Prospection* **21**: 169–183. https://doi.org/10.1002/arp.1480

Papadopoulos NG, Tsourlos P, Tsokas GN et al. 2006. Two-dimensional and three- dimensional resistivity imaging in archaeological site investigation. *Archaeological Prospection* **13**: 163–181. https://doi.org/10.1002/arp.276 [PubMed: 163181

Papadopoulos NG, Tsourlos P, Tsokas GN et al. 2007. Efficient ERT measuring and inversion strategies for 3D imaging of buried antiquities. *Near Surface Geophysics* **5**: 349–361. https://doi.org/10.3997/1873-0604.2007017

Papadopoulos NG, Yi M-J, Kim J-H et al. 2010. Geophysical investigation of tumuli by means of surface 3D electrical resistivity tomography. *Journal of Applied Geophysics* **70**: 192–205. https://doi.org/10.1016/j.jappgeo.2009.12.001

Piroddi L, Calcina SV, Trogu A et al. 2020. Automated Resistivity Profiling (ARP) to explore wide archaeological areas: the prehistoric site of Mont'e Prama, Sardinia, Italy. *Remote Sensing* **12**: 461. https://doi.org/10.3390/rs12030461

Pringle JK, Westerman AR, Schmidt A et al. 2002. Investigating Peak Cavern, Castleton, Derbyshire, UK: integrating cave survey, geophysics, geology and archaeology to create a 3-D digital CAD model. *Cave and Karst Science* **29**: 67–74.

Quarto R, Schiavone D, Diaferia I. 2007. Ground penetrating radar survey of a prehistoric site in Southern Italy. *Journal of Archaeological Science* **34**: 2071–2080. https://doi.org/10.1016/j.jas.2007.02.024

Quinif Y. 2018. Fantomisation et spéléogenèse: implications et questionnement. *Karstologia: revue de karstologie et de spéléologie physique* **69**: 32–46.

Quinif Y, Bruxelles L. 2011. L'altération de type 'fantome de roche': processus, évolution et implications pour la karstification. *Géomorphologie: Relief, Processus, Environnement* **17**: 349–358. https://doi.org/10.4000/geomorphologie.9555

Quinif Y. 2014. La fantomisation – Une nouvelle manière de concevoir la formation des cavernes. *Regards* **N.**79 – Deuxieme semester, 42–72.

Rainone ML, Rusi S, Torrese P. 2015. Mud volcanoes in central Italy: subsoil characterization through a multidisciplinary approach. *Geomorphology* **234**: 228–242. https://doi.org/10.1016/j.geomorph.2015.01.026

Razafindratsima S and Lataste J-F. 2014. Estimation of the error made in Pole-Dipole Electrical Resistivity Tomography depending on the location of the remote electrode: modeling and field study. *Journal of Applied Geophysics* **100**: 44–57. https://doi.org/10.1016/j.jappgeo.2013.10.008

Reimer PJ, Austin WEN, Bard E et al. 2020. The IntCal20 Northern Hemisphere radiocarbon age calibration curve (0–55 cal kBP). *Radiocarbon* **62**: 725–757. https://doi.org/10.1017/RDC.2020.41

Rezaee MR, Motiei H, Kazemzadeh E. 2007. A new method to acquire m exponent and tortuosity factor for microscopically heterogeneous carbonates. *Journal of Petroleum Science and Engineering* **56**: 241–251. https://doi.org/10.1016/j.petrol.2006.09.004

Robain H, Albouy Y, Dabas M et al. 1999. The location of infinite electrodes in pole–pole electrical surveys: consequences for 2-D imaging. *Journal of Applied Geophysics*, **41**(4): 313–333. https://doi.org/10.1016/S0926-9851(99)00010-5

Salem HS, Chilingarian GV. 1999. The cementation factor of Archie's equation for shaly sandstone reservoirs. *Journal of Petroleum Science and Engineering* **23**: 83–93. https://doi.org/10.1016/S0920-;4105(99)00009-1

Sarris A, Kalayci T, Moffat I et al. 2018. An introduction to geophysical and geochemical methods in digital geoarchaeology. In *Digital Geoarchaeology. Natural Science in Archaeology*, Siart C, Forbriger M, Bubenzer O (eds). Springer: Cham.

Sarris A, Papadopoulos N, Soupios S. 2014. Contribution of geophysical approaches to the study of Priniatikos Pyrgos. In *A Cretan Landscape Through Time: Priniatikos Pyrgos and Environs,*

BAR International Series, Molloy BPC, Duckworth CN (eds). **2634**). Archaeopress: Oxford; 61–69.

Satitpittakul A, Vachiratienchai C, Siripunvaraporn W. 2013. Factors influencing cavity detection in Karst terrain on two-dimensional (2-D) direct current (DC) resistivity survey: A case study from the western part of Thailand. *Engineering Geology* **152**: 162–171. https://doi.org/10.1016/j.enggeo.2012.10.015

Sauro U. 2005. Closed depressions. In *Encyclopedia of Caves*, Culver DC, White WB (eds). Elsevier Academic Press: London; 108–122.

Scapozza C, Laigre L. 2014. The contribution of electrical resistivity tomography (ERT) in Alpine dynamics geomorphology: case studies from the Swiss Alps. *Géomorphologie: Relief, Processus, Environnement* **20**: 27–42.

Schmidt AR, Linford P, Linford N et al. 2015 *EAC Guidelines for the Use of Geophysics in Archaeology: Questions to Ask and Points to Consider*. EAC Guidelines 2. Europae Archaeologia Consilium (EAC): Namur, Association Internationale sans But Lucratif (AISBL).

Schrott L, Sass O. 2008. Application of field geophysics in geomorphology: advances and limitations exemplified by case studies. *Geomorphology* **93**: 55–73.

Seaton WJ, Burbey TJ. 2002. Evaluation of two-dimensional resistivity methods in a fractured crystalline-rock terrane. *Journal of Applied Geophysics* **51**: 21–41.

Seno S, Dallagiovanna G, Vanossi M. 2003. Palaeogeography and thrust development in the Pennidic Domain of the Western Alpine chain: examples from the Ligurian Alps. *Bollettino della Società Geologica Italiana* **122**: 223–232.

Shopov Y, Stoykova D, Petrova A et al. 2008. Potential and limitations of the archaeo-geophysical techniques *Proceedings of the International Conference, 29–30 October 2008, Geoarchaeology and Archaeomineralogy, Sofia*, Kostov RI, Gaydarska B, Gurova M (eds). Publishing House "St. Ivan Rilski": Sofia; 320–324.

Simyrdanis K, Papadopoulos N, Kim JH et al. 2015. Archaeological investigations in the shallow seawater environment with electrical resistivity tomography. *Near Surface Geophysics* **13**: 601–611. https://doi.org/10.3997/1873-0604.2015045

Smith DL. 1986. Application of the pole-dipole resistivity technique to the detection of solution cavities beneath highways. *Geophysics* **51**: 833–837. https://doi.org/10.1190/1.1442135

Sola F. 2007. Tesi di Laurea: Geomorfologia carsica del monte Fenera (Vc). Relatore prof. Alfredo Bini, correlatore dr. Stefano Turri, Università degli Studi di Milano – Facoltà di Scienze Matematiche, Fisiche e Naturali, Corso di Laurea in Scienze Geologiche, A.A. 2006–2007 (in Italian, unpublished)

Supriyadi A, Suprianto A, Priyantari N et al. 2019. Assessment of validated geoelectrical resistivity methods to reconstruct buried archaeological site (case study: beteng Site-Sidomekar, Jember Regency). *Journal of Physics: Conference Series* **1153**: 012026. https://doi.org/10.1088/1742-6596/1153/1/012026

Szalai S, Novák A, Szarka L. 2009. Depth of investigation and vertical resolution of surface geoelectric arrays. *Journal of Environmental and Engineering Geophysics* **14**: 15–23. https://doi.org/10.2113/JEEG14.1.15

Szalai S, Szarka L. 2008. Parameter sensitivity maps of surface geoelectric arrays I. Linear arrays. *Acta Geodaetica et Geophysica Hungarica* **43**: 419–437. https://doi.org/10.1556/AGeod.43.2008.4.4

Thacker PT, Ellwood BB, Pereira CMC. 2002. Detecting Palaeolithic activity areas through electrical resistivity survey: an assessment from vale de Óbidos, Portugal. *Journal of Archaeological Science* **29**: 563–570.

Tonkov N. 2014. Geophysical survey at the early Neolithic site of Yabalkovo. In *Yabalkovo vol 1, ATE- Ars et Technica Expicatus*, Roodenberg J, Leshtakov K, Petrova V (eds). Sofia Univeristy 'St. Kliment Ohridski': Sofia; 73–78.

Torrese P. 2020. Investigating karst aquifers: using pseudo 3-D electrical resistivity tomography to identify major karst features. *Journal of Hydrology* **580**. https://doi.org/10.1016/j.jhydrol.2019.124257

Torrese P, Pozzobon R, Rossi AP et al. 2021a. Detection, imaging and analysis of lava tubes for planetary analogue studies using electric methods (ERT). *Icarus* **357**. https://doi.org/10.1016/j.icarus.2020.114244

Torrese P, Zucca F, Martini S *et al.* 2021b. 3D electrical resistivity data collected at Arma Veirana cave (Northern Italy) [Data set]. *Zenodo.* https://doi.org/10.5281/zenodo.4544550

Tsokas GN, Tsourlos PI, Kim JH *et al.* 2018. ERT imaging of the interior of the huge tumulus of Kastas in Amphipolis (northern Greece). *Archaeological Prospection* **25**: 347–361. https://doi.org/10.1002/arp.1718

Tsokas GN, Tsourlos PI, Stampolidis A *et al.* 2009. Tracing a major Roman road in the area of ancient Helike by resistivity tomography. *Archaeological Prospection* **16**: 251–266. https://doi.org/10.1002/arp.355

Van Schoor M. 2002. Detection of sinkholes using 2D electrical resistivity imaging. *Journal of Applied Geophysics* **50**: 393–399.

Waxman MH, Smits LJM. 1968. Electrical conductivities in oil-bearing shaly sands. *Society of Petroleum Engineers Journal* **8**: 107–122.

Witten A. 2017. *Handbook of Geophysics and Archaeology.* Routledge: New York.

Yogeshwar P, Hamacher S, Reçi H *et al.* 2019. Investigating sedimentological architecture using electrical resistivity tomography: A case study from the archaeological open-air site Shën Mitri, Southern Albania. *Pure and Applied Geophysics* **176**: 843–856. https://doi.org/10.1007/s00024-018-1987-6

Zhu J, Currens JC, Dinger JS. 2011. Challenges of using electrical resistivity method to locate karst conduits—A field case in the Inner Bluegrass Region, Kentucky. *Journal of Applied Geophysics* **75**: 523–530.